

Effective Medium Theory for Nonlocal Non-Hermitian Willis Metabeams

Shaoyun Wang

Department of Mechanical and Aerospace Engineering, University of Missouri, Columbia, Missouri 65211, USA

Guoliang Huang*

Department of Mechanics and Engineering Science, College of Engineering, Peking University, Beijing 100871, PR China

Abstract

Unlike classical elasticity, Willis media exhibit coupling between stress–velocity and momentum–strain, capturing additional dynamic interactions in heterogeneous systems. While previous studies have predominantly focused on the homogenization of passive Willis media, extending these concepts to active systems remains largely unexplored. In this work, we develop an effective medium theory (EMT) for nonlocal non-Hermitian Willis metabeams that integrates active sensor–actuator pairs into a background beam to induce nonreciprocal coupling. By employing a source-driven homogenization approach, our EMT accurately captures the full dispersion curves over the entire Brillouin zone—overcoming the limitations of static or long-wavelength theories—and enables the definition of a winding number for the frequency spectrum under periodic boundary conditions (PBC). Notably, our framework predicts the emergence of low-frequency shear waves, absent in traditional beam theory, and facilitates direction-dependent wave amplification and attenuation. Through asymptotic analysis, we determine the frequency spectrum under open boundary conditions (OBC) and reveal its relationship to the periodic spectrum, with the resulting eigenmodes (skin modes) exhibiting pronounced edge localization that can be characterized by the generalized Brillouin zone (GBZ). Furthermore, we establish a bulk–boundary correspondence (BBC) that links the winding number to the localization direction of skin modes, providing a practical alternative to directly computing the GBZ. Finally, we demonstrate applications in nonreciprocal filtering, amplification, and interface-localized energy harvesting, paving the way for next-generation active mechanical metamaterials with tailored wave functionalities.

Keywords: Willis medium, dynamic homogenization, non-Hermiticity, nonlocality, nonreciprocity, topology

1. Introduction

Momentum, a conserved quantity proportional to the product of density and velocity, arises as a consequence of spatial homogeneity according to Noether’s theorem (Landau et al., 1976; Goldstein et al., 2002). In contrast, the stress-strain relation—stating that stress is proportional to an elastic constant times strain—is an empirical law characterizing specific material behavior (Landau et al., 1986). Despite their differing physical origins, momentum–velocity and stress-strain pairs share a fundamental similarity: they both act as conjugate variables in the Lagrangian formalism. Classical elasticity treats them independently, but Willis media introduce cross-

*Corresponding author

Email address: guohuang@pku.edu.cn (Guoliang Huang)

8 couplings—termed Willis couplings—between momentum and strain, as well as stress and velocity, modifying con-
9 ventional elastic behavior (Willis, 1981, 1997). These couplings necessitate new homogenization methods including
10 Green’s function methods and field averaging (Willis, 2009, 2011, 2012; Milton and Willis, 2010; Nemat-Nasser and
11 Srivastava, 2011; Shuvalov et al., 2011; Norris et al., 2012; Srivastava, 2015; Nassar et al., 2015), asymptotic ho-
12 mogenization (Nassar et al., 2016), perturbative expansions combined with field averaging (Qu et al., 2022; Milton,
13 2007), and mode expansion with subspace projection (Ponge et al., 2017; Pernas-Salomón and Shmuel, 2018). Such
14 approaches have extended Willis couplings to acoustics (Muhlestein et al., 2017; Li et al., 2022, 2024) and piezoelec-
15 tricity (Pernas-Salomón and Shmuel, 2020b; Pernas-Salomón et al., 2021; Pernas-Salomón and Shmuel, 2020a; Lee
16 et al., 2023; Baz, 2024; Muñafra et al., 2023). However, homogenization in active systems, where artificial couplings
17 arise, remains challenging. Source-driven homogenization (Sieck et al., 2017) offers a systematic framework for incor-
18 porating background media and scatterers, making it a promising approach for studying active systems. This study
19 extends source-driven homogenization to a non-Hermitian Willis metabeam with sensor–actuator elements, breaking
20 major symmetry (Fig. 1). We develop an effective medium model that captures high-frequency and short-wavelength
21 wave behavior, advancing both theoretical and practical understanding of active Willis materials.

22 Willis media, derived from homogenization theory, exhibit unique properties that drive advanced metamaterial
23 design. In cloaking, transformed media extend beyond classical elasticity and align with the Milton–Briane–Willis
24 gauge (Milton et al., 2006; Chen and Haberman, 2023). Willis coupling enables asymmetric reflection (Liu et al., 2019;
25 Muhlestein et al., 2017) and precise control over polarization, mode conversion, wavefront shaping, and independent
26 reflection/transmission tuning (Qu et al., 2022; Chen et al., 2020; Li et al., 2018). While most studies focus on passive
27 Willis systems, integrating active elements, particularly sensor–actuator pairs, leads to novel effects like direction-
28 dependent wave amplification (Cheng and Hu, 2022) and nonreciprocal wave propagation (Zhai et al., 2019). Despite
29 these advances, key aspects such as non-Hermiticity, topology (bulk–boundary correspondence), symmetry properties,
30 and space–time duality remain largely unexplored (Christensen et al., 2024; Yves et al., 2024; Ashida et al., 2020;
31 Galiffi et al., 2022).

32 In classical elasticity, material properties remain constant (Landau et al., 1986), whereas metamaterials exhibit
33 frequency-dependent properties, enabling effects like bandgaps (Huang et al., 2009) and negative refraction (Zhu
34 et al., 2014). Willis media extend this by introducing both temporal nonlocality (frequency dispersion) and spatial
35 nonlocality (spatial dispersion). While spatial dispersion is well-established in optics—leading to anisotropic prop-
36 agation, gyrotropy, and directed energy flow (Agranovich and Ginzburg, 2013; Shokri and Rukhadze, 2019)—it is
37 uncommon in elasticity. In structured elastic media, it couples material properties to both frequency and wavenum-
38 ber, altering wave interactions. For free waves, effective properties follow dispersion relations, but external loads that
39 depend on both parameters can excite waves with arbitrary frequencies and wavenumbers. This nonlocality is cru-
40 cial for capturing high-frequency and short-wavelength behavior, essential for understanding spectral topology under
41 PBCs and skin modes under OBCs. However, it also complicates boundary value problems by requiring nonlocal
42 boundary conditions.

43 Non-Hermitian systems have advanced significantly since Carl Bender’s discovery that PT-symmetric non-Hermitian
44 operators can have entirely real eigenvalues (Bender and Boettcher, 1998), challenging the notion that Hermiticity is
45 necessary for real spectra (Sakurai and Napolitano, 2017) and expanding research in non-Hermitian physics (Bender

and Hook, 2024). Varying non-Hermitian couplings induces PT-symmetry breaking, leading to a phase transition from real to complex eigenvalues (Ashida et al., 2020). At the transition point (exceptional point), eigenvalues and eigenvectors coalesce, enabling novel effects such as enhanced sensor sensitivity and unconventional laser modes (Miri and Alu, 2019). Simultaneously, the study of topological insulators, rooted in bulk-boundary correspondence, faces challenges in non-Hermitian systems due to the breakdown of Bloch band theory. This leads to non-Bloch band theory and the discovery of the non-Hermitian skin effect (Yao and Wang, 2018), which establishes a new form of bulk-boundary correspondence linking the winding number of the complex frequency spectrum under PBC to skin modes under OBC (Okuma et al., 2020; Zhang et al., 2020). Many quantum non-Hermitian findings extend naturally to classical wave systems, including electromagnetic and acoustic waves, due to their shared mathematical framework—eigenvalue problems in the Hilbert space. Non-Hermitian skin modes appear in elastic systems (Chen et al., 2021), interface modes in metaplates (Wang et al., 2024), and bulk-boundary correspondence in discrete systems (Wu et al., 2024). However, a systematic exploration of the frequency spectrum under both PBC and OBC, particularly the role of the GBZ in governing skin modes and extending bulk-boundary correspondence to nonlocal non-Hermitian Willis systems, remains an open question.

Elastic beams with piezoelectric patches and integrated circuitry serve as a versatile platform for studying unconventional elastic waves. They enable observations of the non-Hermitian skin effect (Chen et al., 2021), odd mass density (Wu et al., 2023), temporal reflection (Wang et al., 2025), frequency conversion (Wu et al., 2022), and topological pumping (Xia et al., 2021). Beam models also advance Willis media research, from dynamic homogenization of inhomogeneous Euler–Bernoulli beams (Pernas-Salomón and Shmuel, 2018) to parameter retrieval in Timoshenko beams with multiple scatterers (Liu et al., 2019; Chen et al., 2020). However, developing a complete EMT for active Timoshenko beams with multiple scatterers remains an open challenge.

Building on the design in Chen et al. (2020), we introduce non-Hermiticity into a background beam by embedding sensor–actuator pairs that generate nonreciprocal coupling (Fig. 2(a)). Using source-driven homogenization, we develop an effective medium theory for nonlocal non-Hermitian Willis metabeam (Fig. 2(b)) and explore its novel phenomena (Fig. 2(c–f)). The main contributions are:

- **Full Dispersion Reproduction:** Captures dispersion curves across the entire Brillouin zone, surpassing static or long-wavelength homogenization limitations.
- **Winding Number Definition:** Establishes a winding number for the frequency spectrum of dispersion curves.
- **Low-Frequency Shear Waves:** Predicts low-frequency shear waves absent in traditional beam theory.
- **Nonreciprocal Wave Control:** Enables direction-dependent wave amplification and attenuation.
- **Asymptotic Frequency Analysis:** Derives the OBC spectrum and its relationship to the PBC spectrum.
- **Skin Modes Characterization:** Identifies edge-localized eigenmodes (skin modes) under OBC, characterized by the GBZ.
- **Bulk–Boundary Correspondence:** Establishes a direct link between the winding number and skin mode localization, avoiding computationally intensive GBZ calculations.

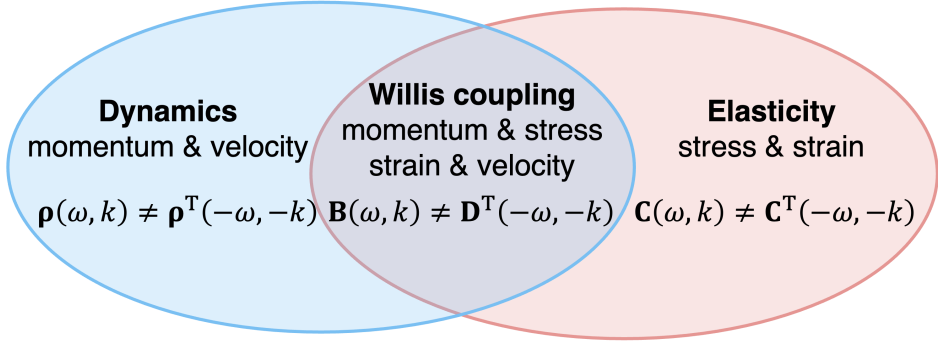


Figure 1: Possible constitutive operators in elastodynamics with broken major symmetry. The broken major symmetry of the elastic tensor $\mathbf{C}(\omega, k) \neq \mathbf{C}^T(-\omega, -k)$, density tensor $\rho(\omega, k) \neq \rho^T(-\omega, -k)$, and Willis coupling tensor $\mathbf{B}(\omega, k) \neq \mathbf{D}^T(-\omega, -k)$ leads to the non-Hermitian media.

- **Practical Applications:** Demonstrates applications in nonreciprocal filters, amplifiers, and interface-localized energy harvesting.

This paper is organized as follows. Section 2 presents the source-driven homogenization approach for nonlocal non-Hermitian Willis metabeams with embedded sensor-actuator elements. Section 3 validates the proposed EMT by comparing theoretical dispersion predictions with COMSOL simulations across various parameter regimes. Section 4 analyzes key wave phenomena, including low-frequency shear waves, nonreciprocal wave amplification and attenuation, asymptotic analysis of the open-boundary spectrum, and bulk–boundary correspondence. Section 5 explores practical applications such as nonreciprocal filtering, amplification, and interface-localized energy harvesting. Finally, Section 6 summarizes the main findings and outlines future research directions. Additional derivations and supporting materials are provided in the Appendices.

2. Effective medium theory of nonlocal non-Hermitian Willis metabeam

In this section, we apply EMT to derive the effective constitutive relations for a metabeam embedded with sensor-actuators (Fig. 2(a)). The homogenization process is illustrated in Fig. 2(b), where sensors and actuators are modeled as embedded scatterers. We first introduce the Timoshenko beam equations (Section 2.1), forming the theoretical foundation. The background beam response under external sources (Fig. 2(b), top panel) is analyzed in Section 2.2, followed by the effective medium response (Fig. 2(b), bottom panel) in Section 2.3. The total response (Fig. 2(b), middle panel), comprising the microscale local response (Section 2.4) and mesoscale multiple scattering effects (Section 2.5), leads to the derivation of the effective constitutive relations (Section 2.6). Finally, we formulate the nonlocal governing equations and boundary value problem (BVP) in Section 2.7.

2.1. Fundamental Equations of the Timoshenko Beam

Consider a Timoshenko beam characterized by mass density ρ , Young's modulus E , and shear modulus G . The material's response is governed by the balance of linear momentum μ and angular momentum J (Yao et al., 2009; Chen et al., 2020)

$$\begin{aligned}\partial_t \mu &= \partial_x F + f, \\ \partial_t J &= \partial_x M + F + q,\end{aligned}\tag{1}$$

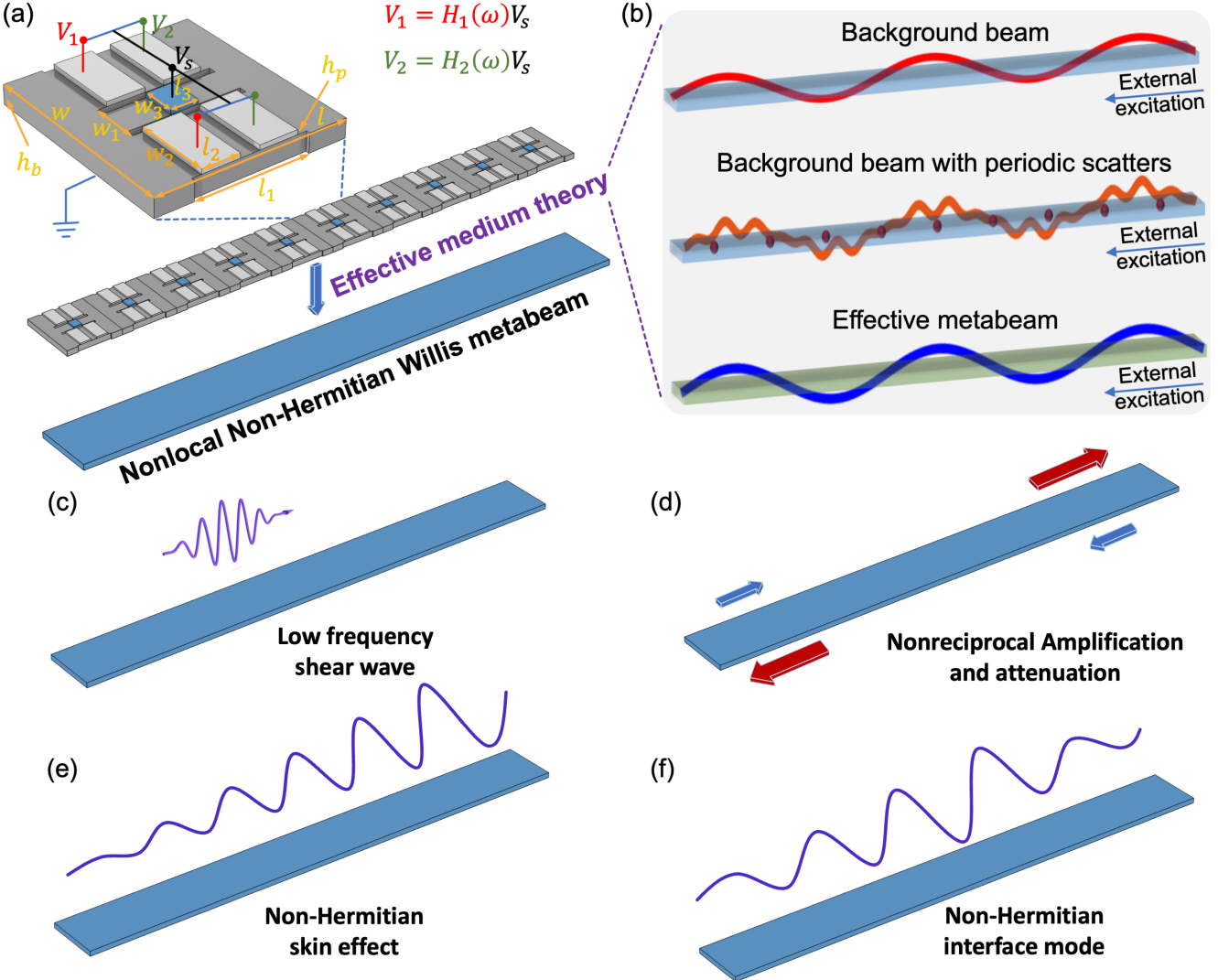


Figure 2: Schematic illustration of the EMT for a metabeam and its associated wave phenomena. (a) The unit cell of the metabeam, featuring a sensor (blue) and four actuators (light gray) in the top panel. The middle panel depicts a finite metabeam consisting of 10 unit cells, while the bottom panel presents its effective medium representation as a nonlocal non-Hermitian Willis metabeam. (b) A schematic diagram illustrating the wave responses in different configurations: the top panel shows the response of the background beam, the middle panel includes periodic scatterers embedded in the background beam, and the bottom panel represents the response of the homogenized effective beam, all under external excitation (blue arrow). (c–f) Demonstrations of various phenomena of the nonlocal non-Hermitian Willis metabeam: (c) low-frequency shear wave propagation, (d) nonreciprocal wave amplification and attenuation, (e) the non-Hermitian skin effect, and (f) the non-Hermitian interface mode.

where F denotes the shear force, M represents the bending moment, and f and q correspond to the external body torque and transverse body force, respectively. The bending curvature κ , shear strain γ , rotational angle ψ , and transverse displacement w satisfy the following geometric relations (Yao et al., 2009; Chen et al., 2020)

$$\begin{aligned}\kappa &= \partial_x \psi + p \\ \gamma &= \partial_x w - \psi + s,\end{aligned}\tag{2}$$

108 where p and s represent the external curvature load and shear load, respectively. The general constitutive relation
109 of the Timoshenko beam is given by (Yao et al., 2009; Chen et al., 2020)

$$\begin{bmatrix} \kappa \\ \gamma \\ \mu \\ J \end{bmatrix} = \begin{bmatrix} 1/D_0 & 0 & 0 & 0 \\ 0 & 1/G_0 & 0 & 0 \\ 0 & 0 & \rho_0 & 0 \\ 0 & 0 & 0 & I_0 \end{bmatrix} \begin{bmatrix} M \\ F \\ \partial_t w \\ \partial_t \psi \end{bmatrix}, \quad (3)$$

110 where D_0 is the bending stiffness, G_0 is the shear stiffness, I_0 is the moment of inertia, and ρ_0 is the line mass density.

111 These parameters are defined as $D_0 = EI$, $G_0 = k_s AG$, $I_0 = \rho I$, and $\rho_0 = \rho A$, where A is the cross-sectional area,
112 k_s is the Timoshenko shear coefficient (taken as 5/6), I is the second moment of area, and ρ is the material density.

113 Using Eqs. (1), (2), and (3), the governing equations can be written in matrix form for the state vector

$$\zeta_1 \mathbf{u} = \mathbf{Q}, \quad (4)$$

114 where

$$\zeta_1 = \begin{bmatrix} 1/D_0 & 0 & 0 & -\partial_x \\ 0 & 1/G_0 & -\partial_x & 1 \\ 0 & \partial_x & -\rho_0 \partial_t^2 & 0 \\ \partial_x & 1 & 0 & -I_0 \partial_t^2 \end{bmatrix}, \quad \mathbf{u} = \begin{bmatrix} M \\ F \\ w \\ \psi \end{bmatrix}, \quad \mathbf{Q} = \begin{bmatrix} p \\ s \\ f \\ q \end{bmatrix}. \quad (5)$$

115 Meanwhile, Eq. (4) in the frequency domain $e^{-i\omega t}$ is

$$\zeta_2 \mathbf{u} = \mathbf{Q}, \quad (6)$$

116 and in frequency-wavenumber domain $e^{i(kx-\omega t)}$ is

$$\zeta \mathbf{u} = \mathbf{Q}, \quad (7)$$

117 where

$$\zeta_2 = \begin{bmatrix} 1/D_0 & 0 & 0 & -\partial_x \\ 0 & 1/G_0 & -\partial_x & 1 \\ 0 & \partial_x & \omega^2 \rho_0 & 0 \\ \partial_x & 1 & 0 & \omega^2 I_0 \end{bmatrix}, \quad \zeta = \begin{bmatrix} 1/D_0 & 0 & 0 & -ik \\ 0 & 1/G_0 & -ik & 1 \\ 0 & ik & \omega^2 \rho_0 & 0 \\ ik & 1 & 0 & \omega^2 I_0 \end{bmatrix} \quad (8)$$

118 2.2. Response of the background beam under external sources

119 Under the external excitation $e^{i(kx-\omega t)}$ shown in the top panel of Fig. 2(b), the governing equations for the state
120 vector of a homogeneous background beam with external sources in the frequency-wavenumber domain are given by
121 (Chen et al., 2020)

$$\zeta \mathbf{u}_{\text{ext}} = \mathbf{Q}_{\text{ext}}, \quad (9)$$

122 where the subscript ext denotes the fields in Eq. (7) under external excitation.

123 2.3. Response of the effective metabeam under external sources

124 For the background beam with periodic scatterers under external excitation, as shown in the middle panel of Fig.
 125 2(b), the response consists of the intrinsic behavior of the background beam and multiple scattering effects induced
 126 by the periodic scatterers. In this setup, actuators generate a source vector, making the scatterers function similarly
 127 to external sources.

128 In the homogenization process, the source vector applied by the actuators is represented as an effective source
 129 vector \mathbf{Q}_{eff} . The governing equations for the state vector of the effective metabeam are then given by (Chen et al.,
 130 2020)

$$\zeta \mathbf{u}_{\text{eff}} + \mathbf{Q}_{\text{eff}} = \mathbf{Q}_{\text{ext}}. \quad (10)$$

131 Here, \mathbf{Q}_{eff} is an unknown vector dependent on the local response at the microscopic scale and the multiple scattering
 132 effects at the mesoscale, both of which are discussed in the following sections.

133 2.4. Local response at microscopic scale

134 The sensor-actuator elements detect the local state vector \mathbf{u}_{loc} and apply the source vector \mathbf{Q}_0 to the beam. The
 135 geometry and material parameters are presented in Appendix A. In our design (Fig. 2(a)), the sensor detects only
 136 the bending curvature, while four actuators apply the bending moment and shear strain. However, this framework
 137 can be extended to systems capable of detecting the complete local state vector and applying the full source vector.
 138 In the frequency domain, the local source vector is related to the local state vector through the polarizability tensor,
 139 modulated by the transfer functions $H_1(\omega)$ and $H_2(\omega)$, as shown in Fig. 2(a) (Chen et al., 2020),

$$\mathbf{Q}_0 = \boldsymbol{\beta}(\omega) \mathbf{u}_{\text{loc}}. \quad (11)$$

140 The tensor $\boldsymbol{\beta}(\omega)$ is a frequency-dependent local polarizability tensor, with only β_{11} and β_{21} being nonzero in our
 141 design, as shown in Fig. 2(a). It is directly linked to the transfer functions implemented via analog or digital circuits
 142 but cannot be determined analytically. Instead, we obtain it using the retrieval method described in the Appendix
 143 E.

144 As shown in Fig. 2(a), the transfer function defines the relationship between the sensed voltage V_s from the
 145 sensing piezoelectric patch and the actuator voltages V_1 and V_2 , given by

$$\begin{aligned} V_1 &= H_1(\omega) V_s, \\ V_2 &= H_2(\omega) V_s. \end{aligned} \quad (12)$$

146 Here, $V_s = \int_A D_z dA / C_0$, where A is the top surface area of the sensing piezoelectric patch, D_z is the z -component
 147 of the electric displacement vector, and C_0 is the capacitance, provided in Appendix A. An example of transfer
 148 function implementation is detailed in Chen et al. (2021).

149 In electrical engineering, a transfer function is generally expressed as the ratio of two complex polynomials. For
 150 instance, the transfer functions $H_1(\omega)$ and $H_2(\omega)$ in this study can be written as

$$H_i(\omega) = \frac{\sum_{m=0}^M a_{m,i} \omega^m}{\sum_{n=0}^N b_{n,i} \omega^n}, \quad i = 1, 2, \quad (13)$$

151 where M and N are the highest-order indices, and $a_{m,i}$ and $b_{n,i}$ are the complex coefficients of the m th and n th
 152 order terms in the numerator and denominator polynomials of $H_i(\omega)$, respectively. The local polarizability tensor
 153 is not directly proportional to the transfer functions; however, its elements remain rational functions, as indicated
 154 by our observations and supported by the strong agreement between EMT predictions and COMSOL simulations.
 155 Consequently, the element in the i th row and j th column can be expressed as

$$\beta_{ij}(\omega) = \frac{\sum_{m=0}^M \tilde{a}_{m,ij}\omega^m}{\sum_{n=0}^N \tilde{b}_{n,ij}\omega^n}, \quad i, j = 1, 2, 3, 4, \quad (14)$$

156 where M and N denote the highest-order indices, and $\tilde{a}_{m,ij}$ and $\tilde{b}_{n,ij}$ are the complex coefficients of the m th
 157 and n th order terms in the numerator and denominator polynomials of $\beta_{ij}(\omega)$, respectively. By leveraging circuit-
 158 based control, each element can be modulated independently, allowing for the realization of an arbitrary local
 159 constitutive matrix that encompasses frequency-dependent responses, positive and negative values, real and imaginary
 160 components, and non-Hermitian configurations.

161 2.5. Multiple scattering at mesoscopic scale

162 Next, we analyze the multiple scattering effect in the middle panel of Fig. 2(b). Using Eq. (B.18), the state
 163 vector response at position x due to a point source $\mathbf{Q}(x') = \delta(x' - nL)\mathbf{Q}_n$ located at $x' = nL$ is given by

$$\mathbf{u}(x) = \mathbf{G}(\omega, x - nL)\mathbf{Q}_n. \quad (15)$$

164 where the Green's function in the frequency domain is defined in Eq. (B.16).

165 The system in this study is periodic, allowing Bloch's theorem to be applied to all fields, including the source
 166 vector \mathbf{Q}_n (Sieck et al., 2017). Therefore, the source vector \mathbf{Q}_n satisfies

$$\mathbf{Q}_n = e^{iknL}\mathbf{Q}_0. \quad (16)$$

167 Therefore, the total local field \mathbf{u}_{loc} at $x = 0$, excited by all sources, is the superposition of the local fields generated
 168 by each individual internal source and the external field \mathbf{u}_{ext}

$$\mathbf{u}_{\text{loc}} = \mathbf{u}_{\text{ext}} + \sum_{n \in \mathbb{Z}} \mathbf{G}(\omega, 0 - nL)\mathbf{Q}_n = \mathbf{u}_{\text{ext}} + \mathbf{S}(\omega, k)\mathbf{Q}_0, \quad (17)$$

169 where the scattering matrix is defined as

$$\mathbf{S}(\omega, k) = \sum_{n \in \mathbb{Z}} \mathbf{G}(\omega, 0 - nL)e^{iknL}. \quad (18)$$

170 Here, the summation includes the current scatter at $n = 0$, unlike previous studies that exclude it to prevent
 171 divergence (Li et al., 2024). In our case, the Green's function remains finite at $n = 0$. Moreover, removing the
 172 effect of the current scatter violates the symmetry constraints in Eqs. (33–37) derived from macroscopic theory. By
 173 applying the symmetry condition of the Green's function in Eq. (C.6), we find that the scattering matrix \mathbf{S} satisfies

¹⁷⁴ the following symmetry properties:

$$\begin{aligned}\mathbf{S}(\omega, k) &= \mathbf{S}^\dagger(\omega, k), \\ \mathbf{S}(\omega, k) &= \mathbf{S}^T(\omega, -k), \\ \mathbf{S}(\omega, k) &= \mathbf{S}^*(-\omega, -k).\end{aligned}\tag{19}$$

¹⁷⁵ Applying Bloch's theorem to the source vector \mathbf{Q}_n in Eq. (16), the scattering matrix becomes

$$\begin{aligned}\mathbf{S}(\omega, k) &= \sum_{n \in \mathbb{Z}} \left[\mathbf{R}_1(-nL) \mathbf{B}_1(-nL)^T e^{-i|nL|k_1} e^{iknL} + \mathbf{R}_2(-nL) \mathbf{B}_2(-nL)^T e^{-|nL|k_2} e^{iknL} \right] \\ &= \mathbf{R}_1(1) \mathbf{B}_1(1)^T \left(\sum_{n=-\infty}^{-1} e^{i(k_1+k)nL} + \frac{1}{2} \right) + \mathbf{R}_1(-1) \mathbf{B}_1(-1)^T \left(\sum_{n=1}^{\infty} e^{i(k-k_1)nL} + \frac{1}{2} \right) \\ &\quad + \mathbf{R}_2(1) \mathbf{B}_2(1)^T \left(\sum_{n=-\infty}^{-1} e^{(k_2+ik)nL} + \frac{1}{2} \right) + \mathbf{R}_2(-1) \mathbf{B}_2(-1)^T \left(\sum_{n=1}^{\infty} e^{(ik-k_2)nL} + \frac{1}{2} \right) \\ &= \mathbf{R}_1(1) \mathbf{B}_1(1)^T \left(\frac{e^{-iL(k_1+k)}}{1 - e^{-iL(k_1+k)}} + \frac{1}{2} \right) + \mathbf{R}_1(-1) \mathbf{B}_1(-1)^T \left(\frac{e^{iL(k-k_1)}}{1 - e^{iL(k-k_1)}} + \frac{1}{2} \right) \\ &\quad + \mathbf{R}_2(1) \mathbf{B}_2(1)^T \left(\frac{e^{-L(k_2+ik)}}{1 - e^{-L(k_2+ik)}} + \frac{1}{2} \right) + \mathbf{R}_2(-1) \mathbf{B}_2(-1)^T \left(\frac{e^{L(ik-k_2)}}{1 - e^{L(ik-k_2)}} + \frac{1}{2} \right).\end{aligned}\tag{20}$$

¹⁷⁶ Here, $\mathbf{R}_1(x)$, $\mathbf{R}_2(x)$, $\mathbf{B}_1(x)$, and $\mathbf{B}_2(x)$ only depend on the sign of the spatial coordinate x . Therefore, their values at ¹⁷⁷ $x = 1$ are used to represent them for positive x , while their values at $x = -1$ are used to represent them for negative ¹⁷⁸ x . In the final step, the geometric series is used

$$\sum_{n=1}^{\infty} y^n = \lim_{N \rightarrow \infty} \sum_{n=1}^N y^n = \lim_{N \rightarrow \infty} \frac{y - y^{N+1}}{1 - y}.\tag{21}$$

¹⁷⁹ The series converges only if the common ratio satisfies $|y| < 1$. Strictly speaking, the magnitude of the common ¹⁸⁰ ratio is equal to 1, causing the series to diverge. In this study, we directly neglect the divergent term y^{N+1} . This ¹⁸¹ approach can be justified by introducing small damping, allowing the wavenumber to have a small imaginary part ¹⁸² such that the common ratio satisfies $|y| < 1$ (Sieck et al., 2017; Shore and Yaghjian, 2007). Subsequently, the limit ¹⁸³ is taken as the damping approaches zero. This procedure is also validated a posteriori, as the dispersion relations ¹⁸⁴ obtained from the effective media closely match those from COMSOL simulation.

¹⁸⁵ 2.6. Effective constitutive relations

¹⁸⁶ Next, we derive the effective constitutive relations. Eliminating the external excitation from Eqs. (9) and (10) ¹⁸⁷ gives

$$\zeta (\mathbf{u}_{\text{eff}} - \mathbf{u}_{\text{ext}}) = -\mathbf{Q}_{\text{eff}}.\tag{22}$$

¹⁸⁸ Additionally, eliminating the local state vector \mathbf{u}_{loc} from Eq. (11) and (17) yields

$$(\mathbf{I} - \beta \mathbf{S}) \mathbf{Q}_0 = \beta \mathbf{u}_{\text{ext}},\tag{23}$$

189 where \mathbf{I} is the 4×4 identity matrix. Additionally, applying spatial averaging, the effective source vector \mathbf{Q}_{eff} relates
 190 to the microscopic point source vector \mathbf{Q}_0 at $x = 0$ as (Sieck et al., 2017; Chen et al., 2020; Alù, 2011)

$$\mathbf{Q}_{\text{eff}} = \frac{1}{l} \int_{-l/2}^{l/2} \delta(x) \mathbf{Q}_0 dx = \frac{\mathbf{Q}_0}{l}, \quad (24)$$

191 where l is the unit cell length. Using Eqs. (22)–(24), we derive the constitutive relation (detailed derivation in the
 192 Appendix D)

$$\mathbf{Q}_{\text{eff}} = \mathbf{K} \mathbf{u}_{\text{eff}}, \quad (25)$$

193 where

$$\mathbf{K} = [l\mathbf{I} - l\beta\mathbf{S} - \beta\zeta^{-1}]^{-1} \beta. \quad (26)$$

194 If β is nonsingular, Eq. (26) simplifies to

$$\mathbf{K} = [l\beta^{-1} - L\mathbf{S} - \zeta^{-1}]^{-1}. \quad (27)$$

195 In Section 2.4, we establish that the local polarizability matrix β can be an arbitrary frequency-dependent but
 196 wavenumber-independent matrix. Here, we constrain it to be a real symmetric matrix and an even function with
 197 respect to ω . Given ζ in Eq. (8), \mathbf{S} in Eq. (18), and β as a real even symmetric matrix, they satisfy the following
 198 symmetry conditions

$$\begin{aligned} \zeta(\omega, k) &= \zeta^*(-\omega, -k), & \mathbf{S}(\omega, k) &= \mathbf{S}^*(-\omega, -k), & \beta(\omega, k) &= \beta^*(-\omega, -k), \\ \zeta(\omega, k) &= \zeta^\dagger(\omega, k), & \mathbf{S}(\omega, k) &= \mathbf{S}^\dagger(\omega, k), & \beta(\omega, k) &= \beta^\dagger(\omega, k), \\ \zeta(\omega, k) &= \zeta^T(\omega, -k), & \mathbf{S}(\omega, k) &= \mathbf{S}^T(\omega, -k), & \beta(\omega, k) &= \beta^T(\omega, -k). \end{aligned} \quad (28)$$

199 Since matrix addition, subtraction, and inversion in Eq. (26) preserve these symmetries, the resulting matrix \mathbf{K} also
 200 satisfies them.

201 Substituting Eq. (25) into Eq. (10) in the absence of an external source and comparing it with Eq. (3), we
 202 propose a general constitutive relation for Willis metabeams in matrix form

$$\begin{bmatrix} \kappa_{\text{eff}} \\ \gamma_{\text{eff}} \\ \mu_{\text{eff}} \\ J_{\text{eff}} \end{bmatrix} = \begin{bmatrix} 1/D_0 + K_{11} & K_{12} & K_{13}/(-i\omega) & K_{14}/(-i\omega) \\ K_{21} & 1/G_0 + K_{22} & K_{23}/(-i\omega) & K_{24}/(-i\omega) \\ K_{31}/(-i\omega) & K_{32}/(-i\omega) & \rho_0 + K_{33}/(-\omega^2) & K_{34}/(-\omega^2) \\ K_{41}/(-i\omega) & K_{42}/(-i\omega) & K_{43}/(-\omega^2) & I_0 + K_{44}/(-\omega^2) \end{bmatrix} \begin{bmatrix} M_{\text{eff}} \\ F_{\text{eff}} \\ v_{\text{eff}} \\ \varphi_{\text{eff}} \end{bmatrix}, \quad (29)$$

203 Here, v_{eff} and φ_{eff} represent the velocity and angular velocity, respectively, satisfying $v_{\text{eff}} = \dot{w}_{\text{eff}}$ and $\varphi_{\text{eff}} = \dot{\psi}_{\text{eff}}$ in
 204 the time domain, and $v_{\text{eff}} = -i\omega w_{\text{eff}}$ and $\varphi_{\text{eff}} = -i\omega \psi_{\text{eff}}$ in the frequency domain. Using these relations, we rewrite
 205 Eq. (29) as

$$\begin{bmatrix} \boldsymbol{\varepsilon} \\ \mathbf{p} \end{bmatrix} = \begin{bmatrix} \mathbf{C} & \mathbf{B} \\ \mathbf{D} & \rho \end{bmatrix} \begin{bmatrix} \boldsymbol{\sigma} \\ \mathbf{v} \end{bmatrix} \quad (30)$$

206 where

$$\boldsymbol{\varepsilon} = \begin{bmatrix} \kappa_{\text{eff}} \\ \gamma_{\text{eff}} \end{bmatrix}, \mathbf{p} = \begin{bmatrix} \mu_{\text{eff}} \\ J_{\text{eff}} \end{bmatrix}, \boldsymbol{\sigma} = \begin{bmatrix} M_{\text{eff}} \\ F_{\text{eff}} \end{bmatrix}, \mathbf{v} = \begin{bmatrix} v_{\text{eff}} \\ \varphi_{\text{eff}} \end{bmatrix}, \quad (31)$$

207 and

$$\begin{aligned} \mathbf{C} &= \begin{bmatrix} -1/D_0 + K_{11} & K_{12} \\ K_{21} & 1/G_0 + K_{22} \end{bmatrix}, & \mathbf{B} &= \begin{bmatrix} K_{13}/(-i\omega) & K_{14}/(-i\omega) \\ K_{23}/(-i\omega) & K_{24}/(-i\omega) \end{bmatrix}, \\ \mathbf{D} &= \begin{bmatrix} K_{31}/(-i\omega) & K_{32}/(-i\omega) \\ K_{33}/(-i\omega) & K_{34}/(-i\omega) \end{bmatrix}, & \boldsymbol{\rho} &= \begin{bmatrix} \rho_0 + K_{33}/(-\omega^2) & K_{34}/(-\omega^2) \\ K_{43}/(-\omega^2) & I_0 + K_{44}/(-\omega^2) \end{bmatrix}. \end{aligned} \quad (32)$$

208 Equation (30) represents the effective constitutive relation in compliance form, where \mathbf{B} and \mathbf{D} are the Willis coupling
209 matrices. The constitutive matrices satisfy the following conditions

$$\begin{aligned} \mathbf{C}(\omega, k) &= \mathbf{C}^*(-\omega, -k), & \mathbf{B}(\omega, k) &= \mathbf{B}^*(-\omega, -k), \\ \mathbf{D}(\omega, k) &= \mathbf{D}^*(-\omega, -k), & \boldsymbol{\rho}(\omega, k) &= \boldsymbol{\rho}^*(-\omega, -k), \end{aligned} \quad (33)$$

$$\mathbf{C}(\omega, k) = \mathbf{C}^\dagger(\omega, k), \quad \mathbf{B}(\omega, k) = -\mathbf{D}^\dagger(\omega, k), \quad \boldsymbol{\rho}(\omega, k) = \boldsymbol{\rho}^\dagger(\omega, k), \quad (34)$$

$$\mathbf{C}(\omega, k) = \mathbf{C}^T(\omega, -k), \quad \mathbf{B}(\omega, k) = \mathbf{D}^T(\omega, -k), \quad \boldsymbol{\rho}(\omega, k) = \boldsymbol{\rho}^T(\omega, -k), \quad (35)$$

212 Using Eq. (33) and Eq. (34), we obtain the following symmetry conditions

$$\mathbf{C}(\omega, k) = \mathbf{C}^T(-\omega, -k), \quad \mathbf{B}(\omega, k) = \mathbf{D}^T(-\omega, -k), \quad \boldsymbol{\rho}(\omega, k) = \boldsymbol{\rho}^T(-\omega, -k), \quad (36)$$

213 Furthermore, using Eq. (35) and Eq. (36), we obtain the following symmetry conditions

$$\mathbf{C}(\omega, k) = \mathbf{C}(-\omega, k), \quad \mathbf{B}(\omega, k) = \mathbf{B}(-\omega, k), \quad \mathbf{D}(\omega, k) = \mathbf{D}(-\omega, k), \quad \boldsymbol{\rho}(\omega, k) = \boldsymbol{\rho}(-\omega, k), \quad (37)$$

214 These five symmetry conditions are not independent; rather, Eq. (33), Eq. (36), and Eq. (37) serve as the
215 fundamental ones in the macroscopic framework, while the remaining two follow from them. Eq. (33) arises from
216 the requirement that all physical fields in classical physics be real-valued (Agranovich and Ginzburg, 2013; Shokri
217 and Rukhadze, 2019). Eq. (36) represents the major symmetry of Willis materials, while Eq. (37) corresponds to
218 time-reversal symmetry (Agranovich and Ginzburg, 2013; Shokri and Rukhadze, 2019; Altman and Suchy, 2011). Eq.
219 (35) follows from the Maxwell-Betti reciprocity theorem, which itself derives from major symmetry and time-reversal
220 symmetry (Agranovich and Ginzburg, 2013; Shokri and Rukhadze, 2019; Pernas-Salomón and Shmuel, 2020b).

221 Our sensor-actuator system can break these symmetry conditions, enabling the realization of unconventional
222 symmetry-broken nonlocal Willis media. For instance, breaking time-reversal symmetry requires violating the cor-
223 responding symmetry of the polarizability tensor, i.e., $\boldsymbol{\beta}(\omega) \neq \boldsymbol{\beta}(-\omega)$, which can be achieved by implementing
224 odd-frequency-dependent transfer functions. Breaking major symmetry or Maxwell-Betti reciprocity requires a non-
225 Hermitian or asymmetric polarizability tensor. By tailoring the polarizability tensor at the microscopic level, EMT
226 allows for the engineering of macroscopic media with arbitrary symmetry-breaking properties.

227 Here, material properties depend on both frequency and wavenumber, indicating that the Willis metabeam ex-

228 exhibits both frequency and spatial dispersion (Agranovich and Ginzburg, 2013). Frequency and wavenumber are
 229 treated as independent variables, as discussed in Appendix F. In the spacetime domain, these dependencies trans-
 230 late into nonlocal constitutive relations, which are expressed in convolution form (Agranovich and Ginzburg, 2013;
 231 Jackson, 2012; Pernas-Salomón and Shmuel, 2020a).

$$\begin{bmatrix} \boldsymbol{\varepsilon}(t, x) \\ \mathbf{p}(t, x) \end{bmatrix} = \int_{-\infty}^t \int_{-\infty}^{\infty} \begin{bmatrix} \mathbf{C}(t, t'; x, x') & \mathbf{B}(t, t'; x, x') \\ \mathbf{D}(t, t'; x, x') & \boldsymbol{\rho}(t, t'; x, x') \end{bmatrix} \begin{bmatrix} \boldsymbol{\sigma}(t', x') \\ \mathbf{v}(t', x') \end{bmatrix} dt' dx' \quad (38)$$

232 If the medium's properties remain constant over time (time-independent), translational symmetry in the time domain
 233 is preserved, making the constitutive matrix dependent only on the time difference $t - t'$ (Agranovich and Ginzburg,
 234 2013). Similarly, if the medium is spatially uniform, all points are equivalent, and the constitutive matrix depends
 235 only on the spatial difference $x - x'$ (Agranovich and Ginzburg, 2013). Under these conditions, we obtain

$$\begin{bmatrix} \boldsymbol{\varepsilon}(t, x) \\ \mathbf{p}(t, x) \end{bmatrix} = \int_{-\infty}^t \int_{-\infty}^{\infty} \begin{bmatrix} \mathbf{C}(t - t', x - x') & \mathbf{B}(t - t', x - x') \\ \mathbf{D}(t - t', x - x') & \boldsymbol{\rho}(t - t', x - x') \end{bmatrix} \begin{bmatrix} \boldsymbol{\sigma}(t', x') \\ \mathbf{v}(t', x') \end{bmatrix} dt' dx' \quad (39)$$

236 The quantity Ψ , representing $\boldsymbol{\varepsilon}$, \mathbf{p} , \mathbf{C} , \mathbf{B} , \mathbf{D} , $\boldsymbol{\rho}$, $\boldsymbol{\sigma}$, and \mathbf{v} , is related in real space and reciprocal space through the
 237 Fourier transform

$$\Psi(t, x) = \frac{1}{2\pi} \int_{-\infty}^{\infty} \int_{-\infty}^{\infty} \Psi(\omega, k) e^{i(kx - \omega t)} dx dt \quad (40)$$

238 and its inverse transform,

$$\Psi(\omega, k) = \frac{1}{2\pi} \int_{-\infty}^{\infty} \int_{-\infty}^{\infty} \Psi(t, x) e^{-i(kx - \omega t)} dk dt \quad (41)$$

239 Since all wave fields in classical physics are real-valued in real space, the Fourier transform satisfies

$$\Psi(\omega, k) = \Psi^*(-\omega, -k). \quad (42)$$

240 This symmetry condition, imposed by physical constraints at the macroscopic scale, aligns with the microscopic
 241 symmetries of the constitutive matrix in Eq. (33).

242 2.7. Governing equations and boundary value problem

243 In this section, we discuss the governing equations and the BVP. For the effective nonlocal non-Hermitian Willis
 244 metabeam, the effective state vector remains governed by Eq. (1) and Eq. (2). Utilizing the constitutive relation in
 245 Eq. (39), the governing equation for the state vector in the space-time domain is expressed as

$$\begin{bmatrix} 0 & -\partial_x \\ -\partial_x & 1 \end{bmatrix} \boldsymbol{\sigma}(t, x) + \int_{-\infty}^t \int_{-\infty}^{\infty} \mathbf{C}(t - t', x - x') \boldsymbol{\sigma}(t', x') + \mathbf{B}(t - t', x - x') \partial_t \mathbf{w}(t', x') dt' dx' = \mathbf{q}_1 \quad (43)$$

$$\begin{bmatrix} 0 & \partial_x \\ \partial_x & 1 \end{bmatrix} \mathbf{w}(t, x) + \partial_t \int_{-\infty}^t \int_{-\infty}^{\infty} \mathbf{D}(t - t', x - x') \boldsymbol{\sigma}(t', x') + \boldsymbol{\rho}(t - t', x - x') \partial_t \mathbf{w}(t', x') dt' dx' = \mathbf{q}_2 \quad (44)$$

247 where $\mathbf{q}_1 = [p_{\text{ext}}, s_{\text{ext}}]^T$ and $\mathbf{q}_2 = [f_{\text{ext}}, q_{\text{ext}}]^T$. In the frequency-wavenumber domain, the governing equations take
248 the form

$$\mathbf{H}\mathbf{u}_{\text{eff}} = \mathbf{Q}_{\text{ext}}, \quad (45)$$

249 where

$$\mathbf{H} = \begin{bmatrix} 0 & 0 & 0 & -ik \\ 0 & 0 & -ik & 1 \\ 0 & ik & 0 & 0 \\ ik & 1 & 0 & 0 \end{bmatrix} + \begin{bmatrix} \mathbf{C} & -i\omega\mathbf{B} \\ -i\omega\mathbf{D} & -\omega^2\boldsymbol{\rho} \end{bmatrix}. \quad (46)$$

250 In the absence of an external source, the dispersion relations are obtained by setting the determinant of the coefficient
251 matrix to zero

$$\det(\mathbf{H}) = 0. \quad (47)$$

252 For each ω and k satisfying the dispersion relations, the corresponding solution \mathbf{u}_{eff} in Eq. (45) represents the
253 eigenvector.

254 For the vibration problem, boundary conditions are required to determine the eigenfrequencies and eigenmodes of
255 the metabeam. Based on the boundary conditions of the conventional Timoshenko beam, the most relevant boundary
256 conditions for the nonlocal non-Hermitian Willis metabeam are listed below

$$\begin{aligned} \text{Fixed : } & \quad w_{\text{eff}} = 0, \quad \psi_{\text{eff}} = 0 \\ \text{Simply supported : } & \quad w_{\text{eff}} = 0, \quad M_{\text{eff}} = 0 \\ \text{Free : } & \quad M_{\text{eff}} = 0, \quad F_{\text{eff}} = 0 \end{aligned} \quad (48)$$

257 In our formalism of Willis media, the bending moment, shear force, displacement, and rotational angle are integrated
258 into a state vector, allowing them to be directly prescribed as boundary conditions. This approach eliminates the
259 challenges of the conventional Willis media framework, which involves second-order derivatives. In the traditional
260 formulation, the nonlocal constitutive relations in Eq. (25) express the bending moment and shear force in terms
261 of displacement and rotational angle, making their boundary conditions nonlocal. As a result, solving nonlocal
262 boundary conditions analytically becomes intractable, requiring advanced numerical methods (Rabczuk et al., 2023).

263 3. Validation of the effective medium theory

264 In this section, we validate the EMT by comparing its predicted dispersion relations with those from unit cell
265 analysis using COMSOL simulations across various transfer functions, including symmetric real, antisymmetric real,
266 asymmetric real, frequency-dependent real, and antisymmetric imaginary cases. By accounting for spatial dispersion
267 effects, the nonlocal EMT accurately captures wave behavior, including nonreciprocal propagation, attenuation, and
268 amplification, even in high-frequency and short-wavelength regimes—where conventional homogenization theories
269 often fail.

270 In our study, the sensing piezoelectric patch detects only the bending curvature, while the actuating piezoelectric
271 patch applies only the bending moment and shear strain. Consequently, only β_{11} and β_{21} are nonzero in the local

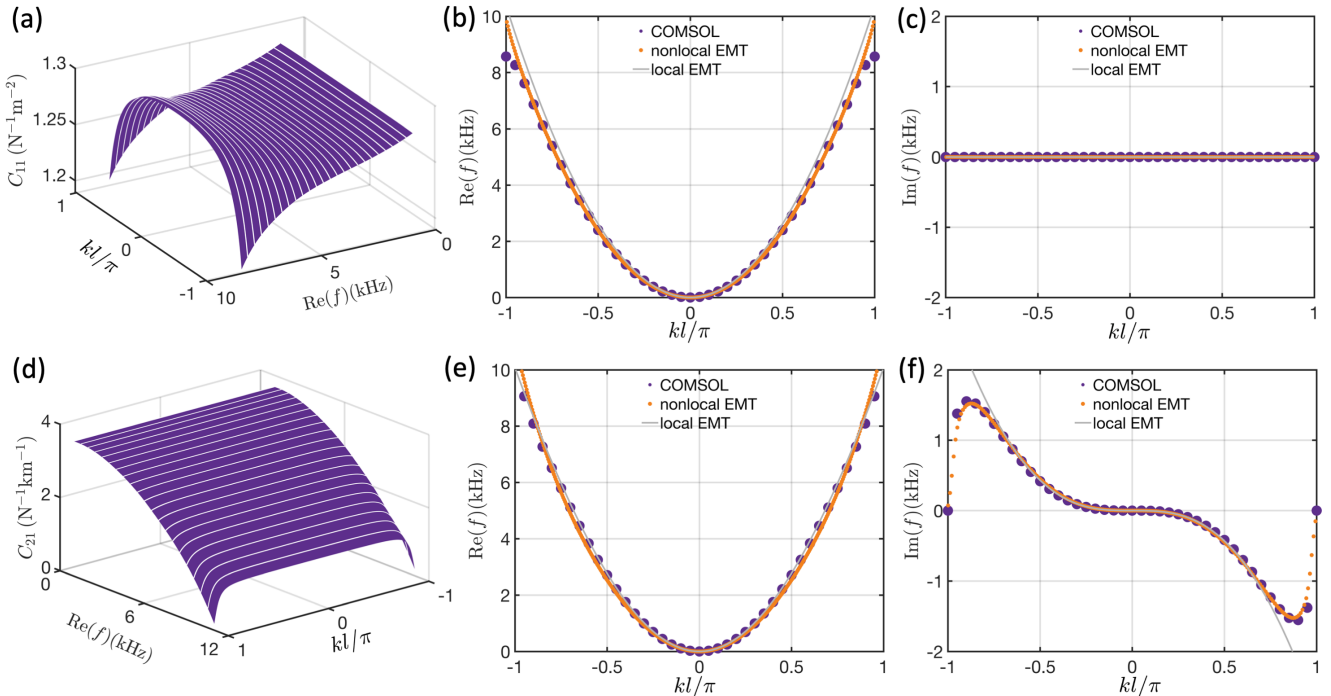


Figure 3: Effective material properties and dispersion relations for symmetric and antisymmetric real transfer functions. (a–c) Symmetric transfer functions: (a) Real part of C_{11} as a function of frequency and wavenumber. (b) Real part of the dispersion curves from unit cell analysis in COMSOL simulations (purple dots), nonlocal EMT (orange dots), and local EMT (gray solid line). (c) Imaginary part of the dispersion curves from COMSOL unit cell analysis (purple dots), nonlocal EMT (orange dots), and local EMT (gray solid line). (d–f) Antisymmetric transfer functions: (d) Real part of C_{21} as a function of frequency and wavenumber. (e) Real part of the dispersion curves from COMSOL unit cell analysis (purple dots), nonlocal EMT (orange dots), and local EMT (gray solid line). (f) Imaginary part of the dispersion curves from COMSOL unit cell analysis (purple dots), nonlocal EMT (orange dots), and local EMT (gray solid line).

²⁷² polarizability tensor. Under this condition, Eq. (26) simplifies to

$$C_{11} = \frac{1}{D_0} + K_{11} \quad (49)$$

$$C_{21} = K_{21},$$

²⁷³ where

$$K_{11} = \frac{\beta_{11}(b_4k^4 + b_2k^2 + b_0)}{a_4k^4 + a_2k^2 + a_1k + a_0} \quad (50)$$

$$K_{21} = \frac{\beta_{21}(b_4k^4 + b_2k^2 + b_0)}{a_4k^4 + a_2k^2 + a_1k + a_0},$$

²⁷⁴ and

$$b_4 = -D_0\beta_{11}g_0$$

$$b_2 = \omega^2(D_0\rho_0 + I_0g_0)$$

$$b_0 = \rho_0\omega^2(-I_0\omega^2 + g_0)$$

$$a_4 = D_0lg_0(-1 + S_{12}\beta_{21} + S_{11}\beta_{11}) \quad (51)$$

$$a_2 = -\omega^2(-D_0l\rho_0 - I_0lg_0 + D_0lS_{12}\beta_{21}\rho_0 + I_0lS_{12}\beta_{21}g_0 + D_0lS_{11}\beta_{11}\rho_0 + D_0I_0\beta_{11}g_0 + I_0lS_{11}\beta_{11}g_0)$$

$$a_1 = -D_0\beta_{21}g_0\omega^2\rho_0i$$

$$a_0 = -\omega^2\rho_0(-I_0\omega^2 + g_0)(-l + lS_{12}\beta_{21} + D_0\beta_{11} + lS_{11}\beta_{11}).$$

²⁷⁵ As $\omega \rightarrow 0$, we also have $k \rightarrow 0$, reducing Eq. (50) to

$$C_{11} = \frac{1}{D_0} + \frac{\beta_{11}}{l - D_0\beta_{11}} \quad (52)$$

$$C_{21} = \frac{\beta_{21}}{l - D_0\beta_{11}},$$

²⁷⁶ Here, the material properties become wavenumber-independent, reducing the medium to a local EMT, accurately
²⁷⁷ matching the dispersion relations in the low-frequency and long-wavelength regime. Additionally, β_{11} influences both
²⁷⁸ C_{11} and C_{21} simultaneously. For small β_{11} , the leading-order term is given by

$$C_{11} = \frac{1}{D_0} + \frac{\beta_{11}}{l} \quad (53)$$

$$C_{21} = \frac{\beta_{21}}{l}.$$

²⁷⁹ In this case, β_{11} and β_{21} independently contribute to C_{11} and C_{21} , respectively.

²⁸⁰ In Eq. (50), K_{11} and K_{21} are proportional to β_{11} and β_{21} , respectively, each scaled by a rational function. For a
²⁸¹ symmetric transfer function where $H_1(\omega) = H_2(\omega)$, the actuators generate only bending moments, making β_{11} the
²⁸² only nonzero component. Consequently, K_{11} is nonzero, modifying the effective bending stiffness in Eq. (30). For an
²⁸³ antisymmetric transfer function where $H_1(\omega) = -H_2(\omega)$, the actuators generate only shear strain, resulting in β_{21} as
²⁸⁴ the only nonzero component. In this case, K_{21} becomes nonzero, leading to the formation of effective shear stiffness
²⁸⁵ in Eq. (30). For an asymmetric transfer function, where $H_1(\omega) \neq H_2(\omega)$ and $H_1(\omega) \neq -H_2(\omega)$, both K_{11} and K_{21}
²⁸⁶ are generated simultaneously. Additionally, in our study, the imaginary part of the rational function is significantly
²⁸⁷ smaller than the real part. As a result, when the transfer functions $H_1(\omega)$ and $H_2(\omega)$ are purely real, K_{11} and K_{21}

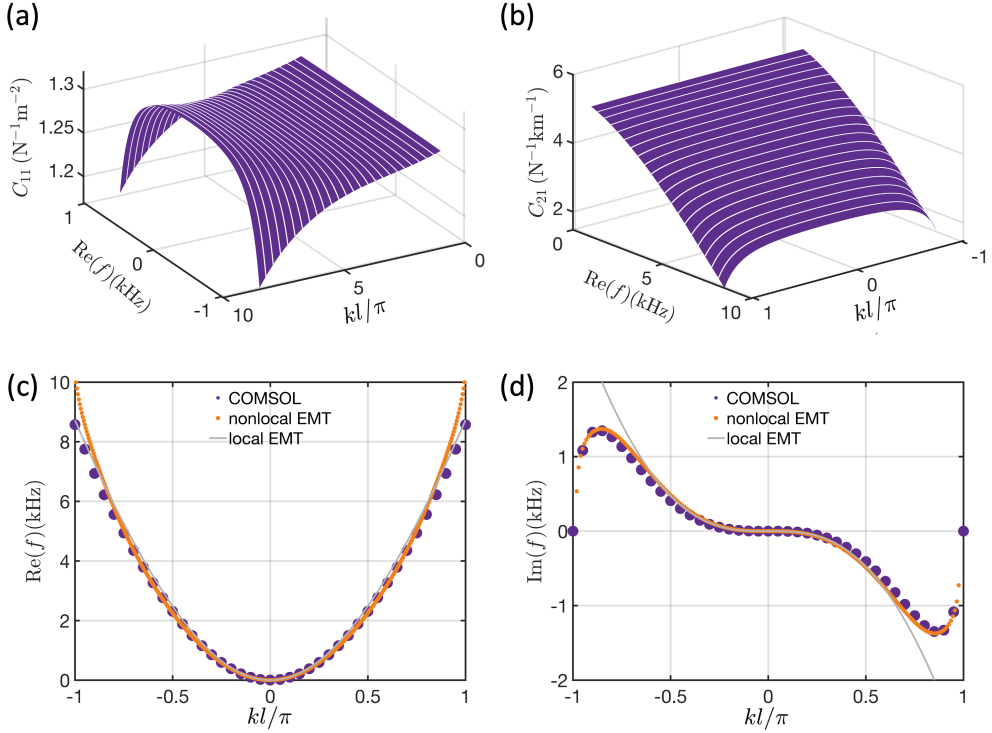


Figure 4: Effective material properties and dispersion relations for asymmetric real transfer functions. (a) Real part of C_{11} as a function of frequency and wavenumber. (b) Real part of C_{21} as a function of frequency and wavenumber. (c) Real part of the dispersion curves from unit cell analysis in COMSOL simulations (purple dots), nonlocal EMT (orange dots), and local EMT (gray solid line). (d) Imaginary part of the dispersion curves from COMSOL unit cell analysis (purple dots), nonlocal EMT (orange dots), and local EMT (gray solid line).

are nearly real. Similarly, when the transfer functions are purely imaginary, K_{11} and K_{21} are nearly imaginary. For complex transfer functions, K_{11} and K_{21} are generally complex-valued.

Next, we examine the effective properties and dispersion relations for different transfer functions. For symmetric transfer functions with $H_1(\omega) = H_2(\omega) = 0.05$, Fig. 3(a) presents the real part of C_{11} , while the imaginary part is omitted as it is negligibly small. The dispersion curves from COMSOL simulations, the nonlocal effective C_{11} from Eq. (49), and the local effective C_{11} from Eq. (52) are shown in Fig. 3(b,c). The dispersion curves from the local EMT align well with COMSOL simulations in the low-frequency and long-wavelength regimes but deviate at high frequencies and short wavelengths. In contrast, the nonlocal EMT provides a close match to the COMSOL results across both low- and high-frequency ranges, demonstrating its superior accuracy in capturing wave dynamics over a broader frequency and wavelength spectrum compared to the local EMT.

For antisymmetric transfer functions with $H_1(\omega) = -H_2(\omega) = 0.3$, the effective properties and dispersion curves are shown in Fig. 3(d-f). Only the real part of C_{21} is displayed, as the imaginary part remains small and is therefore omitted. The presence of a nonzero real C_{21} introduces an imaginary component in the dispersion curves. The local EMT accurately captures both the real and imaginary parts of the dispersion relations in the low-frequency and long-wavelength regimes, while the nonlocal EMT extends this accuracy to high frequencies and short wavelengths. The emergence of C_{21} breaks the major symmetry, rendering the medium non-Hermitian and introducing a nonzero imaginary component in the dispersion relation. Furthermore, the imaginary part of the dispersion relation is antisymmetric with respect to the wavenumber, leading to wave attenuation for left-propagating waves (neg-

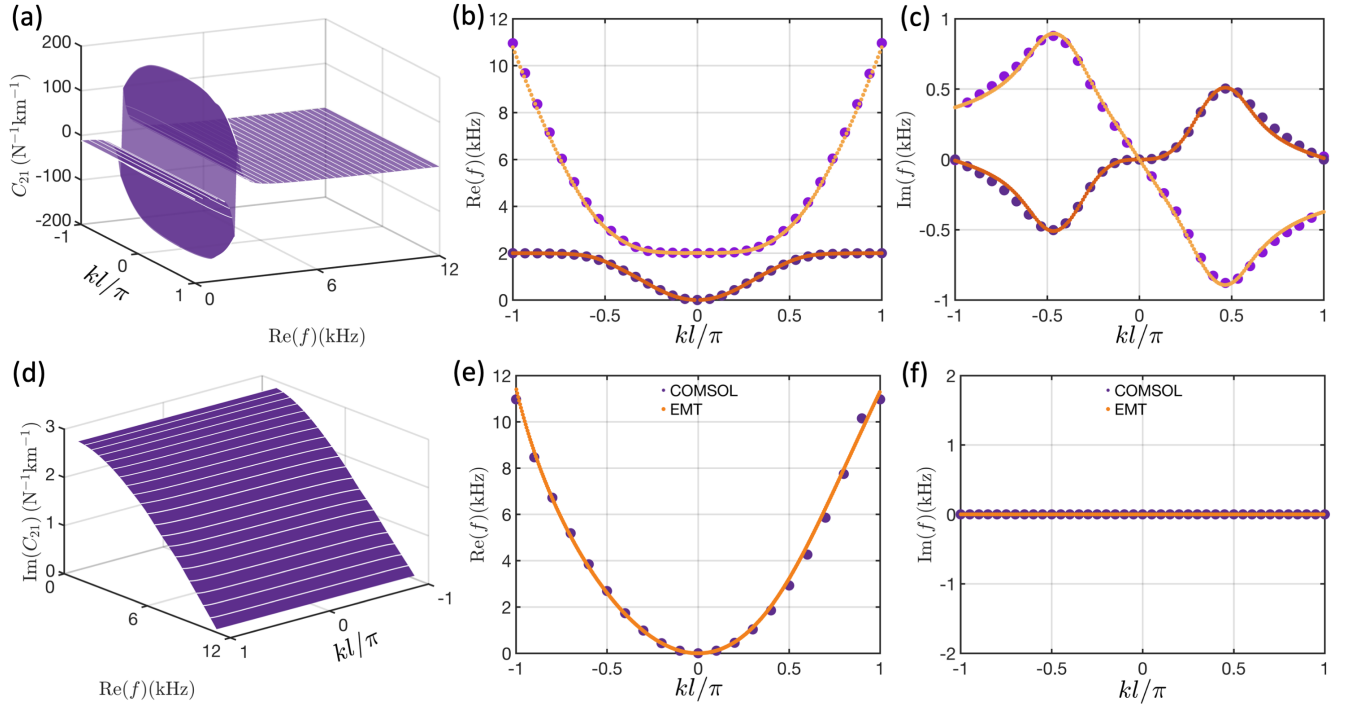


Figure 5: Effective material properties and dispersion relations for local resonant and antisymmetric imaginary transfer functions. (a–c) Local resonant transfer functions: (a) Real part of C_{11} as a function of frequency and wavenumber. (b) Real part of the dispersion curves from COMSOL unit cell analysis (dark purple dots for the lower band, light purple dots for the upper band) and from EMT (dark orange dots for the lower band, light orange dots for the upper band). (c) Imaginary part of the dispersion curves from COMSOL unit cell analysis (dark purple dots for the lower band, light purple dots for the upper band) and EMT (dark orange dots for the lower band, light orange dots for the upper band). (d–f) Antisymmetric imaginary transfer functions: (d) Real part of C_{21} as a function of frequency and wavenumber. (e) Real part of the dispersion curves from COMSOL unit cell analysis (purple dots) and EMT (orange dots). (f) Imaginary part of the dispersion curves from COMSOL unit cell analysis (purple dots) and EMT (orange dots).

tive wavenumber) and amplification for right-propagating waves (positive wavenumber). This asymmetry induces nonreciprocal wave propagation due to non-Hermiticity.

For asymmetric transfer functions with $H_1(\omega) = 0.35$ and $H_2(\omega) = -0.25$, which incorporate the effects of both symmetric and antisymmetric transfer functions, the effective properties and dispersion curves are shown in Fig. 4. In this case, both C_{11} and C_{21} are nonzero, resulting in a downward shift in the real part of the dispersion curve and the appearance of an imaginary component in the dispersion relation. The local EMT accurately captures the dispersion curves in the low-frequency and long-wavelength regimes but shows deviations at high frequencies and short wavelengths. In contrast, the nonlocal EMT closely matches the COMSOL simulation results across both regimes, demonstrating its effectiveness in capturing wave dynamics over a broader frequency and wavelength range.

Our EMT extends beyond constant transfer functions and applies to frequency-dependent transfer functions, including the local resonant transfer function discussed here. We consider antisymmetric transfer functions given by

$$H_1(\omega) = -H_2(\omega) = \frac{0.3\omega_0^2}{\omega^2 - \omega_0^2} \quad (54)$$

where $\omega_0 = 4000\pi$ Hz. In this case, $H_1(\omega)$ is negative for $\omega < \omega_0$, positive for $\omega > \omega_0$, and singular at $\omega = \omega_0$. The antisymmetric transfer function induces a nonzero C_{21} , breaking Hermiticity and resulting in nonzero imaginary dispersion curves. The presence of local resonance splits the dispersion curve into two branches, with the imaginary dispersion curves exhibiting frequency sign reversal due to the sign change of C_{21} at ω_0 . The nonlocal EMT closely

³²¹ matches the COMSOL simulation results for both real and imaginary dispersion curves across high-frequency and
³²² short-wavelength regimes, as shown in Fig. 5(a-c), demonstrating its effectiveness in capturing wave dynamics for
³²³ frequency-dependent transfer functions over a broad frequency and wavelength range.

³²⁴ Non-Hermiticity alone does not necessarily lead to a complex spectrum. For instance, eigenvalues remain real in
³²⁵ the PT-unbroken phase and can also be real in a more general pseudo-Hermitian system (Ashida et al., 2020). In our
³²⁶ system, verifying the pseudo-Hermitian condition is challenging, yet we observe a real spectrum for antisymmetric
³²⁷ imaginary transfer functions. For transfer functions $H_1(\omega) = -H_2(\omega) = 0.3i$, Fig. 5(d) presents the imaginary part
³²⁸ of C_{21} , while the real part is omitted as it is negligibly small. The nonzero C_{21} breaks the Hermitian condition,
³²⁹ yet the spectra in Fig. 5(e,f) remain purely real. However, the real part of the dispersion curve is asymmetric with
³³⁰ respect to the vertical axis, as the nonzero C_{21} breaks parity symmetry. The agreement between the dispersion
³³¹ curves from COMSOL simulations and EMT in Fig. 5(e) confirms this asymmetry, demonstrating the validity of
³³² EMT for purely imaginary transfer functions.

³³³ 4. Wave phenomena in nonlocal non-Hermitian Willis media

³³⁴ 4.1. Low-frequency shear waves

³³⁵ In our study, only K_{21} and K_{11} are nonzero. Thus, the dispersion equations in Eq. (45) simplify to

$$\begin{pmatrix} C_{11} & 0 & 0 & -ki \\ C_{21} & 1/G_0 & -ki & 1 \\ 0 & ki & \omega^2 \rho_0 & 0 \\ ki & 0 & 0 & J_0 \omega^2 \end{pmatrix} \begin{pmatrix} M_{\text{eff}} \\ F_{\text{eff}} \\ w_{\text{eff}} \\ \psi_{\text{eff}} \end{pmatrix} = \begin{pmatrix} 0 \\ 0 \\ 0 \\ 0 \end{pmatrix} \quad (55)$$

³³⁶ where C_{11} and C_{21} are defined in Eq. (49). Eliminate M_{eff} and F_{eff} gives

$$\begin{bmatrix} -C_{11}(-\omega^2 \rho_0 + G_0 k^2) & -G_0 k(C_{11}i - C_{21}k) \\ C_{11}G_0 k i & -C_{11}G_0 + C_{11}J_0 \omega^2 - C_{21}G_0 k i - k^2 \end{bmatrix} \begin{bmatrix} w_{\text{eff}} \\ \psi_{\text{eff}} \end{bmatrix} = \begin{bmatrix} 0 \\ 0 \end{bmatrix} \quad (56)$$

³³⁷ Assuming w_{eff} as 1, we have

$$\psi_{\text{eff}} = -\frac{C_{11}G_0 k i}{C_{11}G_0 - C_{11}J_0 \omega^2 + C_{21}G_0 k i + k^2} \quad (57)$$

³³⁸ The ratio of shear strain and rotation angle is defined as

$$\frac{\gamma_{\text{eff}}}{\psi_{\text{eff}}} = \frac{i k w_{\text{eff}} - \psi_{\text{eff}}}{\psi_{\text{eff}}} = -\frac{(C_{11}i - C_{21}k)(-C_{11}\omega^2 \rho_0 + 2C_{11}G_0 k^2 + C_{21}G_0 k^3 i)}{C_{11}(-\omega^2 \rho_0 + G_0 k^2)(C_{11} + C_{21}k)i} \quad (58)$$

³³⁹ As shown in Fig. 6, the magnitude of the ratio of shear strain to rotation angle increases significantly compared to the
³⁴⁰ traditional Timoshenko beam model, making the shear effect observable when C_{21} is nonzero for the antisymmetric
³⁴¹ transfer functions $H_1 = -H_2 = -1$. This indicates that the Willis metabeam in our study can support shear waves
³⁴² at low frequencies, a feature absent in classical beam models.

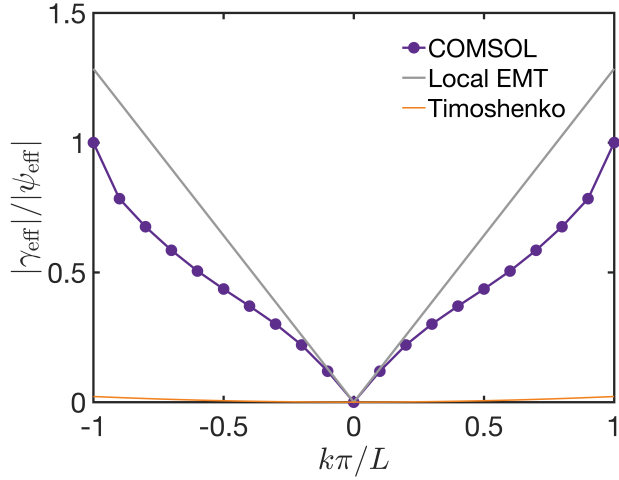


Figure 6: The magnitude of the ratio of shear strain to rotation angle from COMSOL simulations (purple solid line with circles), local EMT (gray solid line), and the traditional Timoshenko beam model (orange solid line). Here, antisymmetric transfer functions $H_1 = -H_2 = 1$ are used.

343 4.2. *Broken the reciprocity theorem*

344 In local media, the reciprocity theorem is equivalent to major symmetry ([Nassar et al., 2020](#)). However, in
345 nonlocal media, major symmetry alone does not ensure reciprocity. Instead, reciprocity arises from the combined
346 presence of major symmetry and time-reversal symmetry ([Shokri and Rukhadze, 2019](#)). In our system, the presence
347 of C_{21} breaks major symmetry, leading to reciprocity violation. Next, we examine reciprocity and its breaking,
348 starting with the Green's function. The Green's function of Willis metabeam in the frequency-wavenumber domain
349 satisfies

$$\mathbf{HG}_{\text{eff}}(\omega, k) = \mathbf{I}. \quad (59)$$

350 The presence of C_{21} breaks the symmetry condition of \mathbf{H} .

$$\mathbf{H}(\omega, k) \neq \mathbf{H}^T(\omega, -k), \quad (60)$$

351 Therefore, the Green's function $\mathbf{G}_{\text{eff}} = \mathbf{H}^{-1}$ no longer satisfies the symmetry condition

$$\mathbf{G}_{\text{eff}}(\omega, k) \neq \mathbf{G}_{\text{eff}}^T(\omega, -k), \quad (61)$$

352 which translates to

$$\mathbf{G}_{\text{eff}}(\omega, x - x') \neq \mathbf{G}_{\text{eff}}^T(\omega, x' - x) \quad (62)$$

353 in the spatial domain. For an external load \mathbf{Q}_{ext} , the corresponding response is given by

$$\mathbf{u}_{\text{eff}}(\omega, x) = \int_L \mathbf{G}_{\text{eff}}(\omega, x - x') \mathbf{Q}_{\text{ext}}(x') dx' \quad (63)$$

354 in the spatial domain. To evaluate the reciprocity condition, we conduct two load-response tests. In the first case, the
355 applied load is $\mathbf{Q}_{\text{ext}}^1(\omega, x)$ with the corresponding response $\mathbf{u}_{\text{eff}}^1(\omega, x)$, while in the second case, the load is $\mathbf{Q}_{\text{ext}}^2(\omega, x)$

356 with the response $\mathbf{u}_{\text{eff}}^2(\omega, x)$. The reciprocity condition is given by (Nassar et al., 2020)

$$\int_L (\mathbf{u}_{\text{eff}}^2)^T(\omega, x) \mathbf{Q}_{\text{ext}}^1(\omega, x) dx = \int_L (\mathbf{u}_{\text{eff}}^1)^T(\omega, x) \mathbf{Q}_{\text{ext}}^2(\omega, x) dx. \quad (64)$$

357 Using Eq. (62), the reciprocity condition can be rewritten as

$$\int_L \int_L (\mathbf{Q}_{\text{ext}}^2)^T(\omega, x') \mathbf{G}_{\text{eff}}^T(\omega, x - x') \mathbf{Q}_{\text{ext}}^1(\omega, x) dx dx' = \int_L \int_L (\mathbf{Q}_{\text{ext}}^1)^T(\omega, x') \mathbf{G}_{\text{eff}}^T(\omega, x - x') \mathbf{Q}_{\text{ext}}^2(\omega, x) dx dx'. \quad (65)$$

358 Taking the transpose and interchanging x and x' on the right-hand side, we obtain

$$\int_L \int_L (\mathbf{Q}_{\text{ext}}^2)^T(\omega, x') \mathbf{G}_{\text{eff}}^T(\omega, x - x') \mathbf{Q}_{\text{ext}}^1(\omega, x) dx dx' = \int_L \int_L (\mathbf{Q}_{\text{ext}}^2)^T(\omega, x') \mathbf{G}_{\text{eff}}(\omega, x' - x) \mathbf{Q}_{\text{ext}}^1(\omega, x) dx dx'. \quad (66)$$

359 Therefore, Eq. (66) shows that the reciprocity condition in Eq. (64) is equivalent to the symmetry condition of the
360 Green's function,

$$\mathbf{G}_{\text{eff}}(\omega, x - x') = \mathbf{G}_{\text{eff}}^T(\omega, x' - x). \quad (67)$$

361 In our study, the presence of C_{21} breaks this symmetry condition, leading to the inequality in Eq. (62). As a result,
362 the equality in Eq. (66) is violated, thereby breaking the reciprocity theorem in Eq. (64).

363 We now numerically verify the breaking of the reciprocity theorem using COMSOL simulations with constant
364 antisymmetric transfer functions $H_1(\omega) = -H_2(\omega) = 0.3$. Two numerical tests are performed: in the first case, a
365 unit shear force $\mathbf{Q}_{\text{ext}}^1(x) = [0, 0, 0, 1]^T \delta(x + 6l)$ is applied at $x = -6l$, and the resulting displacement w_1 is measured
366 at $x = 6l$, as shown in Fig. 7(a). In the second case, a unit shear force $\mathbf{Q}_{\text{ext}}^2(x) = [0, 0, 0, 1]^T \delta(x - 6l)$ is applied at
367 $x = 6l$, and the displacement w_2 is measured at $x = -6l$, as illustrated in Fig. 7(a). The difference between the
368 left-hand side and right-hand side of Eq. (64) is given by

$$\Delta = (\mathbf{u}_{\text{eff}}^2)^T \mathbf{Q}_{\text{ext}}^1 - (\mathbf{u}_{\text{eff}}^1)^T \mathbf{Q}_{\text{ext}}^2 = w_2 - w_1. \quad (68)$$

369 The measured magnitude of Δ , normalized by $|w_2|$, as a function of frequency is shown in Fig. 7(b). Since $|\Delta|/|w_1|$
370 is nonzero, Δ does not vanish, confirming the violation of the reciprocity theorem.

371 For a shear load applied on the left, the wave in the metabeam undergoes attenuation. This attenuation can be
372 characterized using the k - ω dispersion relations. By sweeping ω from 1 kHz to 10 kHz, the corresponding k values
373 are obtained by solving Eq. (47). The resulting dispersion curves are shown in Fig. 7(c) (3D view), Fig. 7(d) (front
374 view), and Fig. 7(e) (top view). As an example, at an excitation frequency of 4 kHz, the imaginary parts of both
375 wavenumbers are positive, indicating wave attenuation in the metabeam, as shown in the top panel of Fig. 7(a).
376 Furthermore, in Fig. 7(f), the imaginary wavenumber matches the decay factor observed in the logarithmic plot of
377 the transverse displacement magnitude, confirming the attenuation behavior.

378 4.3. Bulk-boundary correspondence

379 In Hermitian systems, the governing operator is Hermitian, ensuring real eigenvalues. In classical elasticity, for
380 example, the governing equation can be expressed as an eigenvalue problem in Hilbert space, where the Hermitian

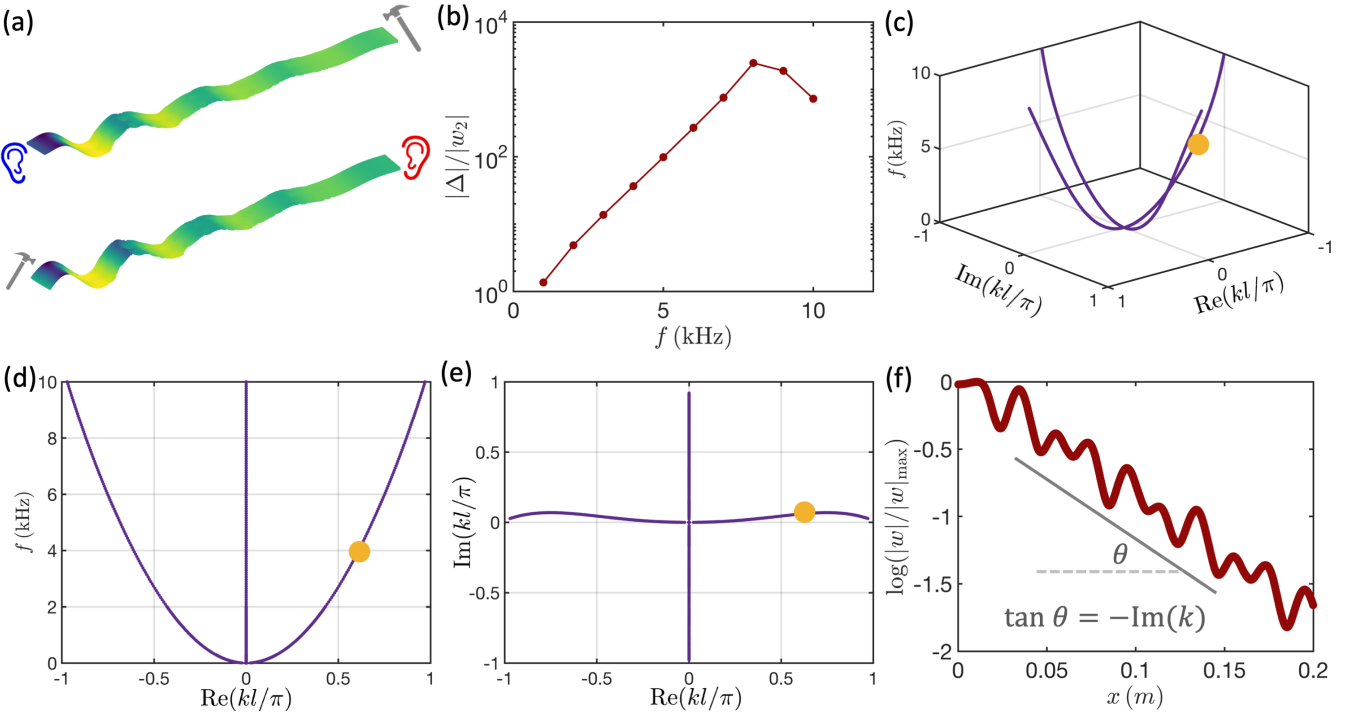


Figure 7: Nonreciprocal wave propagation in Willis media. (a) Displacement response under two shear force loads applied at the right (top panel) and left (bottom panel) with an excitation frequency of 4 kHz. The corresponding displacements are measured at the opposite ends. (b) Normalized displacement difference as a function of excitation frequency. (c) 3D view of the k - ω dispersion curves, where the orange point corresponds to the excitation frequency of 4 kHz in the bottom panel of (a). (d) Front view of the k - ω dispersion curves. (e) Top view of the k - ω dispersion curves. (f) Displacement field extracted along the middle line of the bottom panel in (a), with the slope of the gray solid line corresponding to the imaginary part of the orange point in (e).

381 nature of the operator guarantees real frequency spectrum. However, in non-Hermitian systems, this condition no
 382 longer holds, allowing complex frequency spectrum to emerge.

383 Despite the presence of non-Hermiticity, Bloch's theorem remains valid for systems that maintain linearity and
 384 periodicity. Consequently, the dispersion relation is still well-defined, and non-Hermitian systems exhibit frequency
 385 periodicity in both the real and imaginary axis within the first Brillouin zone. As a result, the frequency spectrum
 386 under PBC forms closed loops in the complex plane, each characterized by a topological invariant known as the
 387 winding number, which arises from differential geometry.

388 Under OBC, non-Hermitian systems exhibit the "skin effect", where most eigenmodes localize near the boundaries,
 389 forming "skin modes" (Yao and Wang, 2018). Studies (Okuma et al., 2020; Yang et al., 2020) show that the existence
 390 and localization direction of these modes are governed by the winding number: a nonzero winding number indicates
 391 the presence of skin modes, while its sign determines their localization direction. This relationship establishes a new
 392 form of bulk-boundary correspondence unique to non-Hermitian physics.

393 In the following section, we outline the method for calculating the winding number of the frequency spectrum
 394 under PBC, conduct an asymptotic analysis to derive the frequency spectrum under OBC, and extend the non-
 395 Hermitian bulk-boundary correspondence to Willis media.

396 4.3.1. Winding number of the frequency spectrum under PBC

397 In our system, multiple eigenfrequencies, denoted as $\omega_\alpha(k)$, may exist for a given wavenumber under PBC. In
 398 non-Hermitian systems, the frequency spectrum is generally complex and can form a loop enclosing a base point ω_b .

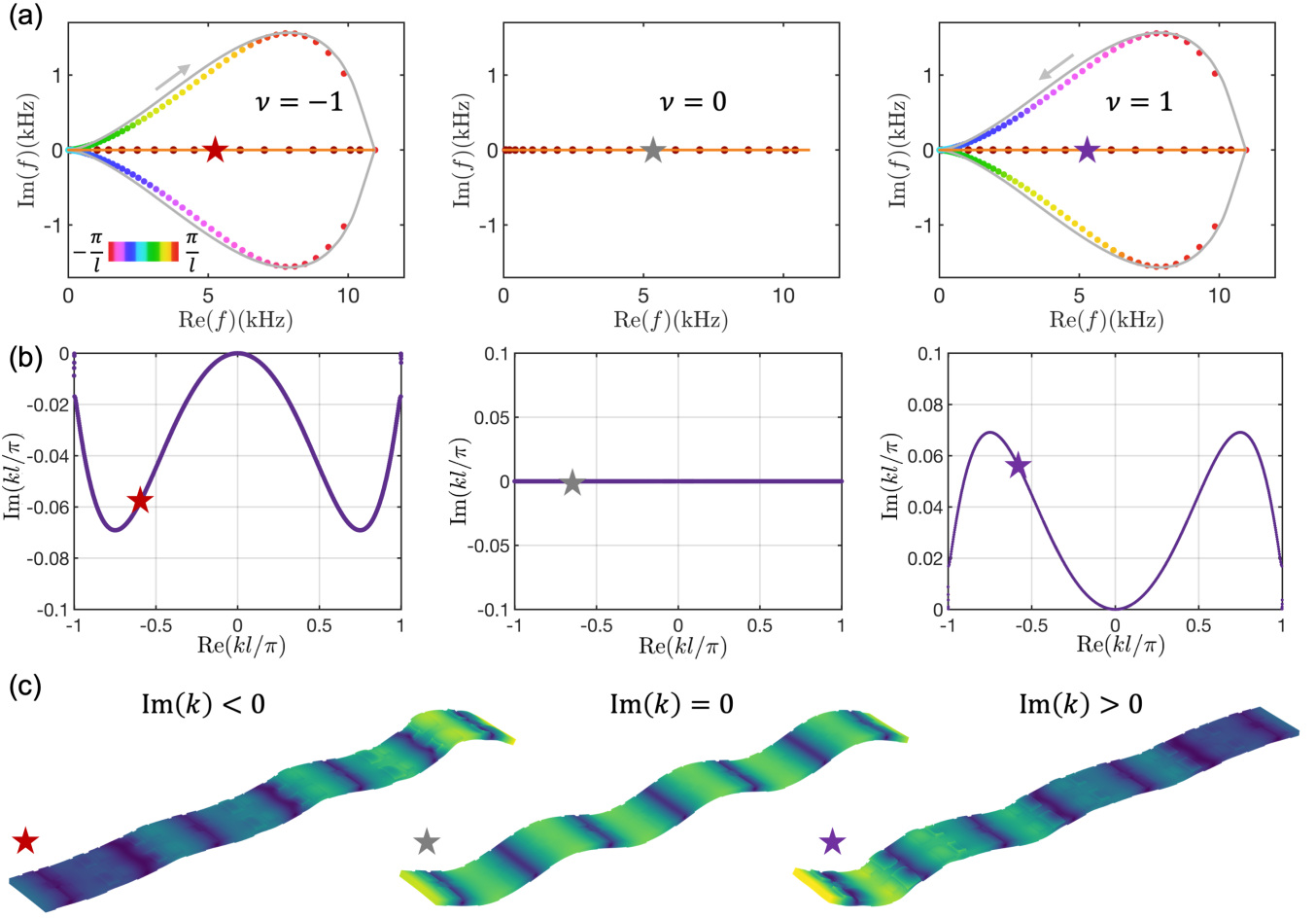


Figure 8: Bulk-boundary correspondence of the winding number and skin mode. (a) Frequency spectrum for the flexural mode of a metabeam under PBC (gradient-colored dots) and fixed boundary conditions (red dots) from COMSOL simulations. The gray solid loop, obtained from the dispersion relation in Eq. (47), and the orange solid line, derived from the BVP in Eq. (78), represent the effective non-Hermitian Willis medium. (b) GBZ associated with the frequency spectrum under fixed boundary conditions, represented by the orange solid line in (a). (c) Eigenmodes from COMSOL simulations corresponding to the starred locations in the frequency spectrum and their associated GBZs. In (a–c), the transfer functions are $H_1 = -H_2 = 0.3$ in the left panel, $H_1 = -H_2 = 0$ in the middle panel, and $H_1 = -H_2 = -0.3$ in the right panel.

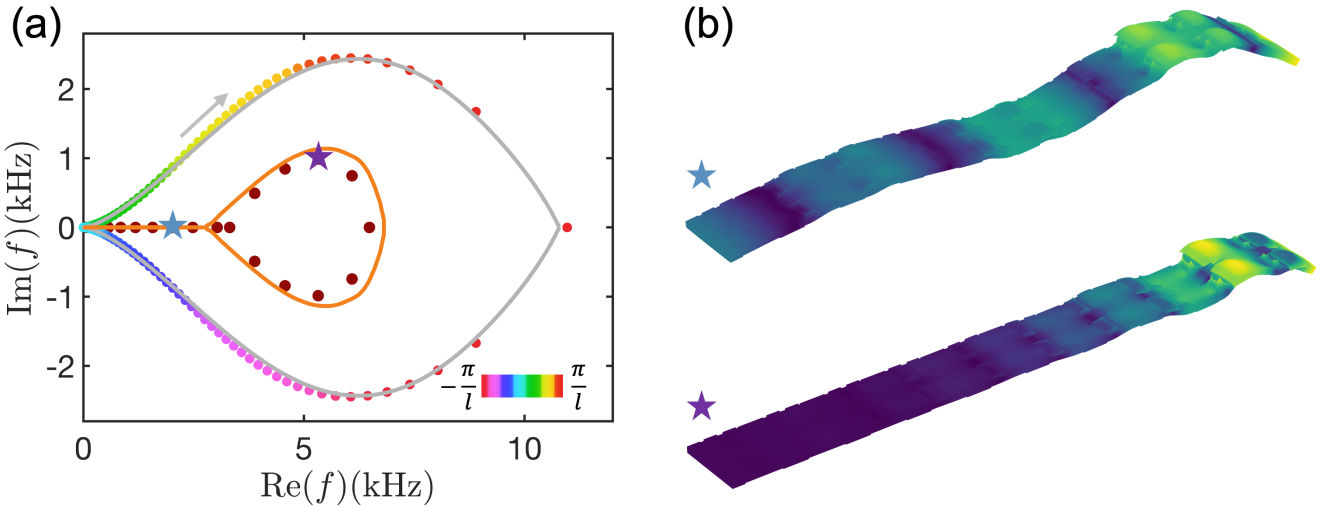


Figure 9: Bulk-boundary correspondence of the winding number and skin mode for transfer functions $H_1(\omega) = -H_2(\omega) = 1$. (a) Frequency spectrum for the flexural mode of a metabeam under PBC (gradient-colored dots) and fixed boundary conditions (red dots) from COMSOL simulations. The gray solid loop, obtained from the dispersion relation in Eq. (47), and the orange solid line, derived from the BVP in Eq. (78), represent the effective non-Hermitian Willis medium. (b) Eigenmodes from COMSOL simulations corresponding to the starred locations in the frequency spectrum (a).

399 This loop remains topologically protected as long as ω_b remains inside it. In one-dimensional systems, such loops
400 are quantitatively characterized by the winding number of the spectrum (Ashida et al., 2020), given by

$$\nu(\omega_b) = \sum_{\alpha} \int_{-\pi/l}^{\pi/l} \frac{dk}{2\pi} \frac{d}{dk} \arg [\omega_{\alpha}(k) - \omega_b]. \quad (69)$$

401 For antisymmetric transfer functions $H_1(\omega) = -H_2(\omega)$, the complex frequency spectrum under PBC is shown in
402 Fig. 8(a) for $H_1(\omega) = 0.3$ (left panel), $H_1(\omega) = 0$ (middle panel), and $H_1(\omega) = -0.3$ (right panel). In the left panel,
403 the spectral loop rotates clockwise as k varies from $-\pi/l$ to π/l , yielding a winding number $\nu(\omega_b) = -1$ for any
404 base frequency ω_b enclosed by the loop. In the middle panel, the frequency spectrum collapses to a line, indicating
405 a winding number of zero for any ω_b . In the right panel, the spectral loop rotates counterclockwise as k varies from
406 $-\pi/l$ to π/l , resulting in a winding number $\nu(\omega_b) = 1$ for any base frequency ω_b inside the loop.

407 For antisymmetric transfer functions $H_1(\omega) = -H_2(\omega) = 1$, the complex frequency spectrum under PBC is shown
408 in Fig. 9(a). The spectrum forms a clockwise loop, indicating a winding number $\nu(\omega_b) = -1$ for any base frequency
409 ω_b enclosed by the loop. When the antisymmetric transfer function follows Eq. (54), the complex frequency spectrum
410 under PBC is shown in Fig. 10(a). In this case, the spectrum consists of a counterclockwise loop on the left and a
411 clockwise loop on the right. Consequently, the winding number $\nu(\omega_b)$ is 1 for any base frequency ω_b inside the left
412 loop and -1 for any base frequency inside the right loop.

413 4.3.2. Asymptotic analysis of the frequency spectrum under OBC

414 Next, we address the BVP for a finite beam with specified boundary conditions. While non-Hermiticity often
415 introduces significant complexity, an intriguing simplification emerges when the beam becomes very long: in this
416 limit, the BVP effectively becomes independent of the specific boundary conditions. That is, for $L \rightarrow \infty$, certain
417 non-Hermitian complexities are mitigated compared to the Hermitian case. In this section, we apply asymptotic
418 analysis to determine the frequency spectrum under OBC by taking the beam's length L to infinity. This approach

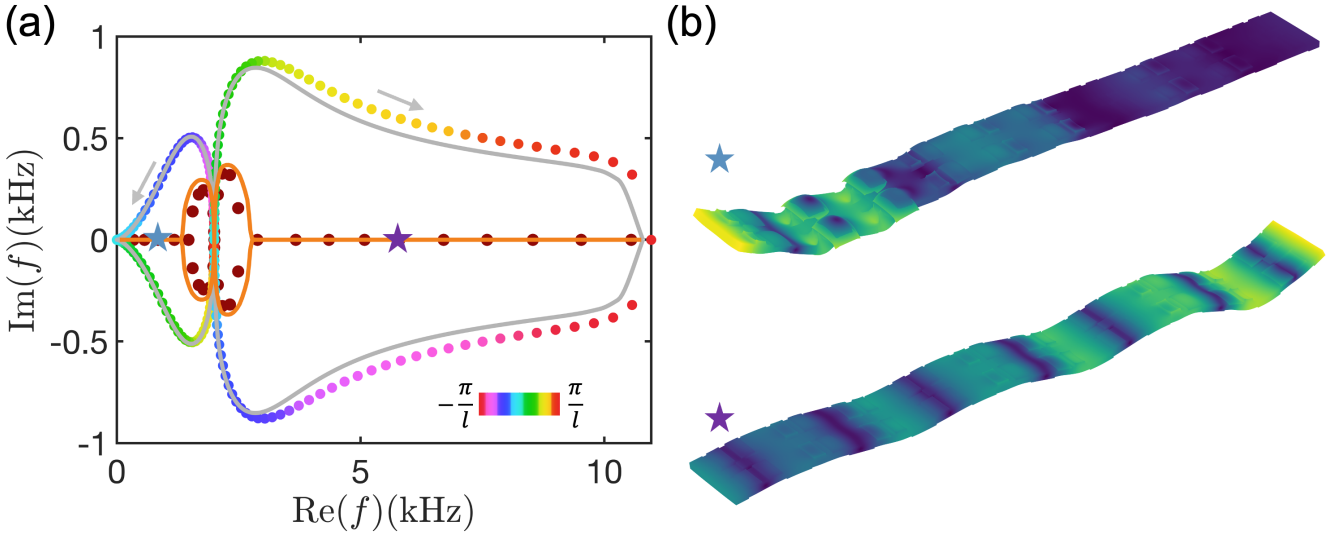


Figure 10: Frequency-dependent skin mode and its bulk-boundary correspondence for transfer functions in Eq. (54). (a) Frequency spectrum for the flexural mode of a metabeam under PBC (gradient-colored dots) and fixed boundary conditions (red dots) from COMSOL simulations. The gray solid loop, obtained from the dispersion relation in Eq. (47), and the orange solid line, derived from the BVP in Eq. (78), represent the effective non-Hermitian Willis medium. (b) Eigenmodes from COMSOL simulations corresponding to the starred locations in the frequency spectrum in (a).

419 yields two algebraic equations whose solutions not only provide the OBC frequency spectrum but also identify the
 420 GBZ—a concept unique to non-Hermitian systems. All derivations in this section are based on EMT, so the subscript
 421 eff is omitted for clarity.

422 For the non-Hermitian medium, the dispersion relation in Eq. (47) yields four wavenumber roots for a given
 423 frequency, denoted as k_n for $n = 1, 2, 3, 4$. The general solution for the transverse displacement of the non-Hermitian
 424 Willis metabeam is given by

$$w(x) = \sum_{n=1}^4 A_n e^{ik_n x} \quad (70)$$

425 where A_n are the corresponding coefficients. The rotational angle is expressed as

$$\psi(x) = \sum_{n=1}^4 A_n R_\psi^n e^{ik_n x} \quad (71)$$

426 where R_ψ^n is defined in Eq. (B.13). Now, we consider the BVP using fixed boundary conditions as an example:

$$w(0) = 0, \quad \psi(0) = 0, \quad w(L) = 0, \quad \psi(L) = 0. \quad (72)$$

427 where L is the length of the finite metabeam. Substituting the wave solutions into these boundary conditions, we
 428 obtain the following equations

$$\begin{pmatrix} 1 & 1 & 1 & 1 \\ R_\psi^1 & R_\psi^2 & R_\psi^3 & R_\psi^4 \\ e^{ik_1 L} & e^{ik_2 L} & e^{ik_3 L} & e^{ik_4 L} \\ R_\psi^1 e^{ik_1 L} & R_\psi^2 e^{ik_2 L} & R_\psi^3 e^{ik_3 L} & R_\psi^4 e^{ik_4 L} \end{pmatrix} \begin{pmatrix} A_1 \\ A_2 \\ A_3 \\ A_4 \end{pmatrix} = \begin{pmatrix} 0 \\ 0 \\ 0 \\ 0 \end{pmatrix} \quad (73)$$

429 Setting the determinant of the coefficient matrix to zero yields the frequency spectrum under fixed boundary conditions
 430

$$\begin{vmatrix} 1 & 1 & 1 & 1 \\ R_\psi^1 & R_\psi^2 & R_\psi^3 & R_\psi^4 \\ e^{ik_1 L} & e^{ik_2 L} & e^{ik_3 L} & e^{ik_4 L} \\ R_\psi^1 e^{ik_1 L} & R_\psi^2 e^{ik_2 L} & R_\psi^3 e^{ik_3 L} & R_\psi^4 e^{ik_4 L} \end{vmatrix} = 0 \quad (74)$$

431 Next, we derive the GBZ by extending the method developed for lattice systems (Yokomizo and Murakami, 2019).
 432 The solution of Eq. (74) simplifies for large L , forming the corresponding continuum spectrum. Expanding the
 433 determinant in Eq. (74), we obtain

$$F_1(\vec{k}, \omega) e^{i(k_1+k_2)L} + F_2(\vec{k}, \omega) e^{i(k_1+k_3)L} + F_3(\vec{k}, \omega) e^{i(k_1+k_4)L} \\ + F_4(\vec{k}, \omega) e^{i(k_2+k_3)L} + F_5(\vec{k}, \omega) e^{i(k_2+k_4)L} + F_6(\vec{k}, \omega) e^{i(k_3+k_4)L} = 0 \quad (75)$$

434 Here, $\vec{k} = [k_1, k_2, k_3, k_4]$, and $F_i(\vec{k}, \omega)$ ($i = 1, 2, \dots, 6$) are coefficients that depend on both frequency and wavenumbers,
 435 obtained by expanding the determinant in Eq. (74). We now analyze the asymptotic behavior of the solutions
 436 of Eq. (75) for large L , where the wavenumbers are ordered as $\text{Im}(k_1) < \text{Im}(k_2) < \text{Im}(k_3) < \text{Im}(k_4)$ for convenience.

437 If $\text{Im}(k_2) \neq \text{Im}(k_3)$, only one leading term proportional to $F_6(\vec{k}, \omega) e^{i(k_3+k_4)L}$ remains in Eq. (75) in the limit of
 438 large L . This leads to

$$F_6(\vec{k}, \omega) = 0 \quad (76)$$

439 which does not depend on L and does not allow for a continuous frequency spectrum.

440 On the other hand, when $\text{Im}(k_2) = \text{Im}(k_3)$, two leading terms proportional to $e^{i(k_2+k_4)L}$ and $e^{i(k_3+k_4)L}$ remain,
 441 allowing Eq. (75) to be rewritten as

$$e^{i(k_2-k_3)L} = -\frac{F_6(\vec{k}, \omega)}{F_5(\vec{k}, \omega)} \quad (77)$$

442 In such a case, we can expect that the difference between $\text{Re}(k_2)$ and $\text{Re}(k_3)$ can be changed almost continuously
 443 for a large L , producing continuum frequency spectrum.

444 Finally, in the asymptotic limit $L \rightarrow \infty$, the boundary value problem of the nonlocal non-Hermitian metabeam
 445 reduces to two algebraic equations:

$$|\mathbf{H}(\omega, k)| = 0, \\ \text{Im}(k_2(\omega)) = \text{Im}(k_3(\omega)). \quad (78)$$

446 For a given complex frequency ω , the first equation in Eq. (78) yields four frequency-dependent wavenumbers $k_1(\omega)$,
 447 $k_2(\omega)$, $k_3(\omega)$, and $k_4(\omega)$, ordered as $\text{Im}(k_1) < \text{Im}(k_2) < \text{Im}(k_3) < \text{Im}(k_4)$. Among these, the second and third
 448 wavenumbers satisfy the second equation in Eq. (78). The first equation is complex and can be decomposed into two
 449 real equations, yielding a total of three real equations involving four independent real variables: $\text{Re}(\omega)$, $\text{Im}(\omega)$, $\text{Re}(k)$,
 450 and $\text{Im}(k)$. As a result, the solutions $(\text{Re}(\omega), \text{Im}(\omega), \text{Re}(k), \text{Im}(k))$ form continuous curves in the four-dimensional
 451 space. When projected onto the complex ω -plane, these solutions appear as continuous curves, ensuring that the
 452 frequency spectrum remains continuous. Similarly, their projection onto the complex k -plane forms continuous curves,
 453 known as the GBZ. The GBZ extends the Brillouin zone concept from Hermitian physics and plays a fundamental

454 role in non-Hermitian physics. It is crucial for reconstructing the bulk-boundary correspondence of the Chern number
455 and topological edge modes, as well as for computing the Green's function to determine system responses, such as
456 stress or strain, under external excitations in engineering applications.

457 As mentioned earlier, Eq. (78) includes a complex equation. Unlike in non-Hermitian local media, where dis-
458 persion relations can be transformed into polynomial equations and efficiently solved using resultant-based methods
459 from algebraic geometry, the dispersion relations here are transcendental. Consequently, the resultant-based method
460 fails, necessitating direct numerical solutions. However, solving complex equations numerically is challenging since
461 many numerical methods are designed for real-valued equations. To address this, for a given variable such as $\text{Re}(\omega)$,
462 Eq. (78) can be reformulated as three real equations involving three real independent unknowns. Numerical tech-
463 niques such as Newton's method, iterative solvers, or gradient-based optimization can then be applied. Here, we
464 use "fsolve" function in MATLAB. By sweeping $\text{Re}(\omega)$ over the desired range, continuous frequency spectra and
465 generalized Brillouin zones can be obtained.

466 In deriving Eq. (78), fixed boundary conditions were used. However, in the asymptotic limit, the frequency
467 spectrum equation in Eq. (78) remains independent of the specific boundary conditions. For other boundary
468 conditions, such as free, simply supported, or mixed conditions, the coefficients $F_i(\vec{k}, \omega)$ ($i = 1, 2, \dots, 6$) will change,
469 but the spectrum condition $\text{Im}(k_2(\omega)) = \text{Im}(k_3(\omega))$ remains unaffected. Therefore, the frequency spectrum can be
470 determined by solving Eq. (75) regardless of the boundary conditions. In other words, the frequency spectrum under
471 OBC is independent of the specific type of boundary conditions.

472 The frequency spectra under OBC for various transfer functions are shown as orange solid lines in Fig. 8(a), Fig.
473 9(a), and Fig. 10(a), closely matching the eigenfrequencies obtained from COMSOL simulations (red dots). Minor
474 discrepancies arise due to the finite beam length in the COMSOL model and diminish as the beam length increases.
475 The corresponding eigenmodes, shown in Fig. 8(c), Fig. 9(b), and Fig. 10(b), exhibit localization at the edges and
476 are therefore identified as skin modes. These skin modes display exponential localization, with exponential factors
477 determined by the GBZ. For instance, the GBZ corresponding to the frequency spectrum in Fig. 8(a) is shown in
478 Fig. 8(b). In the left panel of Fig. 8(b), the GBZ is below the horizontal axis, indicating positive exponential factors,
479 leading to eigenmodes that grow from left to right, as seen in the left panel of Fig. 8(c). In the middle panel of Fig.
480 8(b), the GBZ lies on the horizontal axis, signifying zero exponential factors, corresponding to extended eigenmodes,
481 as shown in the middle panel of Fig. 8(c). In the right panel of Fig. 8(b), the GBZ is above the horizontal axis,
482 indicating negative exponential factors, resulting in eigenmodes that grow from right to left, as depicted in the right
483 panel of Fig. 8(c).

484 4.3.3. Bulk-boundary correspondence

485 In the previous sections, we introduced the methods for calculating the winding number and the frequency
486 spectrum under OBC, along with the concept of skin modes. In this section, we unify these concepts through
487 bulk-boundary correspondence.

488 Bulk-boundary correspondence has two key aspects. The first concerns the relationship between the frequency
489 spectra under PBC and OBC, which holds for both EMT and COMSOL simulations. In non-Hermitian systems, the
490 OBC spectrum is always enclosed by the PBC spectrum. As shown in Fig. 8(a), for small transfer functions, the
491 OBC spectrum remains real and is encircled by the PBC spectrum. As the transfer function magnitude increases,

492 the OBC spectrum becomes complex while still remaining enclosed by the PBC spectrum, as seen in Fig. 9(a). For
493 resonant transfer functions in Fig. 10(a), the PBC spectrum splits into two separate loops, each enclosing the OBC
494 spectrum. These cases illustrate the fundamental relationship between the PBC and OBC spectra, reinforcing the
495 principles of bulk-boundary correspondence in non-Hermitian systems.

496 The second aspect of bulk-boundary correspondence describes the relationship between the sign of the winding
497 number at a base frequency (the eigenfrequency of an eigenmode under OBC) and the localization direction of skin
498 modes. If the winding number at a base frequency is negative, the corresponding skin mode localizes at the right
499 edge, as shown in the left panels of Fig. 8(a,c). If the winding number is zero, the eigenmode remains extended, as
500 depicted in the middle panels of Fig. 8(a,c). Conversely, if the winding number is positive, the skin mode localizes at
501 the left edge, as shown in the right panels of Fig. 8(a,c). These relationships hold for different transfer functions, as
502 further demonstrated in Fig. 9 and Fig. 10. Instead of computing the GBZ, which is complex and computationally
503 demanding, bulk-boundary correspondence provides a more efficient way to determine the localization of skin modes.
504 By simply checking the sign of the winding number from the PBC spectrum, the localization behavior of skin modes
505 can be directly inferred.

506 5. Application

507 5.1. Nonreciprocal filtering and amplification

508 In conventional designs, filters and amplifiers are treated as separate components that cannot be directly inte-
509 grated. However, as shown in the previous section, our system exhibits direction-dependent gain: waves traveling
510 from left to right are amplified, while those traveling from right to left are attenuated. This nonreciprocal property,
511 enabled by Willis media, allows filtering and amplification to be seamlessly integrated into a single metabeam.

512 Specifically, for constant antisymmetric transfer functions $H_1(\omega) = -H_2(\omega) = 0.3$, the dispersion curves in Fig.
513 11(c–e) show that waves always decay from left to right but are amplified from right to left. As a result, when a
514 signal enters from the left, the measured output on the right is attenuated, whereas a signal entering from the right
515 is amplified on the left. By simply switching the input and detection positions, the metabeam can function either
516 as a filter or an amplifier. The frequency responses for these two cases are compared in Fig. 11(a), clearly showing
517 that the right output is attenuated for a left-side input, while the left output is amplified for a right-side input.

518 While conventional frequency-selective filters attenuate signals within a specific passband while leaving out-of-
519 band signals largely unchanged, many applications require the additional capability to amplify out-of-band signals.
520 Our Willis metabeam achieves this dual functionality by utilizing antisymmetric local resonant transfer functions (see
521 Eq. (54)). Specifically, a left-to-right traveling wave is amplified for frequencies below 2 kHz but attenuated above
522 2 kHz, functioning as a low-stop high-amplifying filter (LSHAF). By reversing the input and output positions, the
523 system instead operates as a low-amplifying high-stop filter (LAHSF), amplifying low-frequency components while
524 attenuating higher frequencies. Numerical results for these two modes, shown in Fig. 11(b) and Fig. 11(c), confirm
525 the expected behaviors of LSHAF and LAHSF. Together, these designs offer a novel approach to frequency-selective
526 filtering and amplification, surpassing the capabilities of conventional high-pass or bandpass filters.

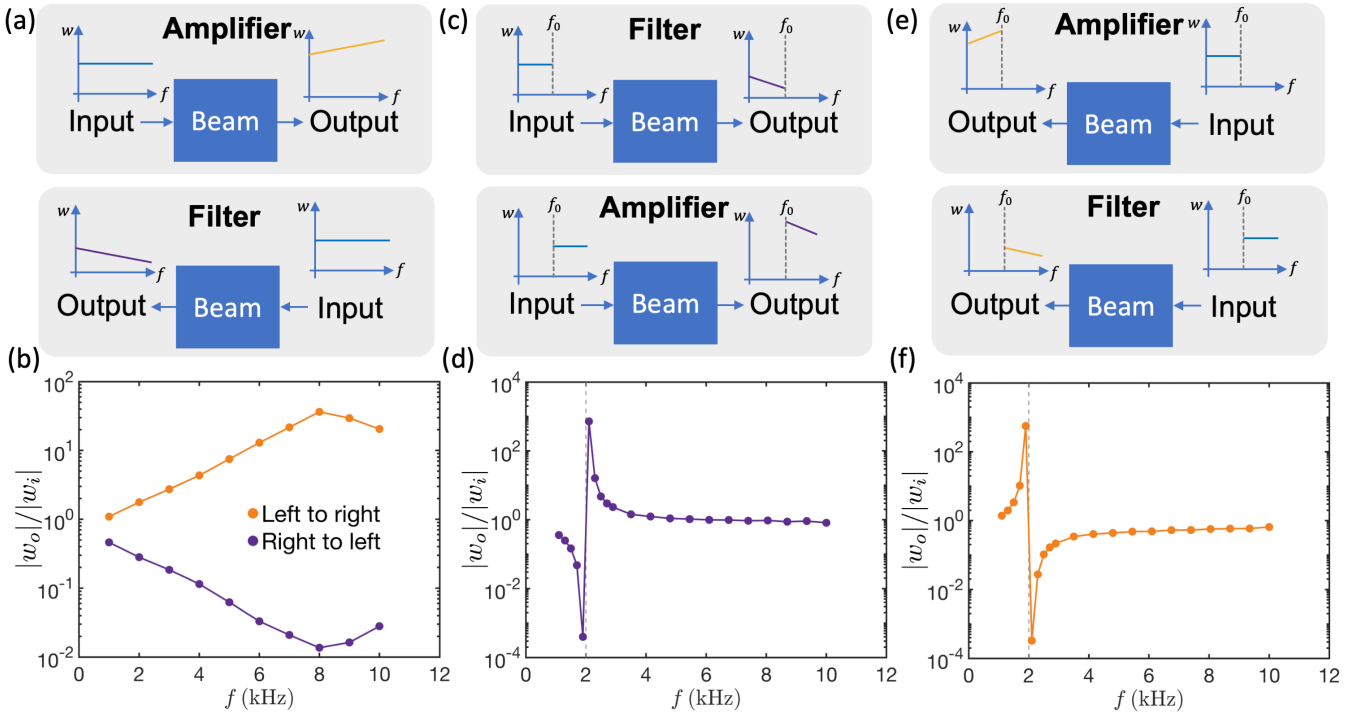


Figure 11: Utilizing nonreciprocal wave behavior for filtering and amplification. (a) For constant antisymmetric transfer functions, the Willis beam amplifies signals propagating from left to right while acting as a filter for signals traveling from right to left. (b) The ratio of output w_o to input w_i signal as a function of excitation frequency for (a). (c) For resonant antisymmetric transfer functions, the Willis beam filters out low-frequency signals (below f_0) and amplifies high-frequency signals (above f_0) when the signal is input from the left and output at the right. (d) The ratio of output w_o to input w_i signal as a function of excitation frequency for (c), with the dashed gray line indicating the resonant frequency $f_0 = 2\text{ kHz}$. (e) For resonant antisymmetric transfer functions, the Willis beam filters out high-frequency signals (above f_0) and amplifies low-frequency signals (below f_0) when the signal is input from the right and output at the left. (f) The ratio of output w_o to input w_i signal as a function of excitation frequency for (e), with the dashed gray line marking the resonant frequency $f_0 = 2\text{ kHz}$.

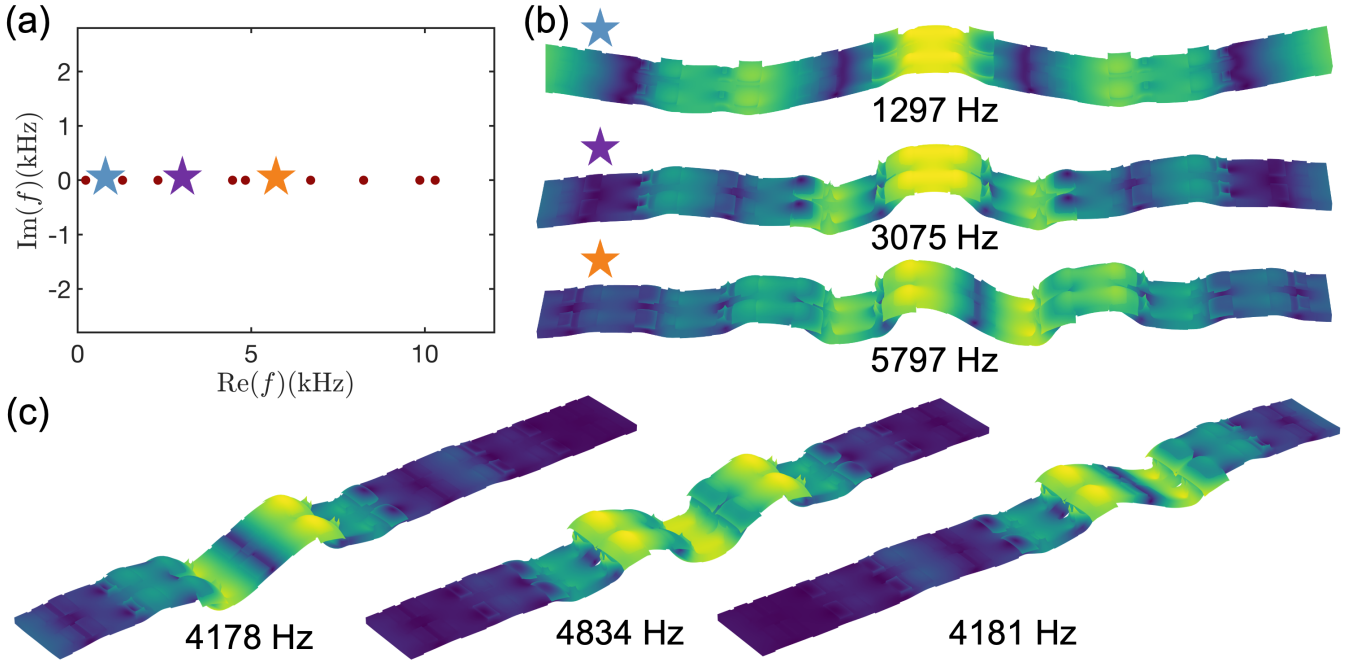


Figure 12: Non-Hermitian interface modes. (a) The frequency spectrum of a finite beam with 10 unit cells, where the interface is located at the 5th and 6th unit cells. The transfer functions for the left five unit cells are $H_1 = -H_2 = -0.3$, while for the right five unit cells, they are $H_1 = -H_2 = 0.3$. (b) Eigenmodes and their corresponding eigenfrequencies at the starred locations in the frequency spectrum of (a). (c) Eigenmodes and their eigenfrequencies for interfaces located between the 3rd and 4th unit cells (left panel), between the 5th and 6th unit cells (middle panel), and between the 7th and 8th unit cells (right panel).

527 5.1.1. Non-Hermitian interface modes and its potential application in energy harvest

528 In energy harvesting, external energy sources are often distributed across a broad area, while the harvester itself
529 is confined to a single location. Efficiently channeling energy from multiple source points to the harvester presents
530 a significant challenge. One approach to address this is through skin modes with a real-valued spectrum, where the
531 real spectrum ensures system stability and prevents unwanted energy feedback from the sensor-actuator circuit into
532 the beam. These modes naturally concentrate energy along a boundary, regardless of the source location, allowing
533 the harvester to be placed there for effective energy collection. However, boundary localization inherently limits
534 the flexibility of harvester placement. To overcome this constraint, we utilize non-Hermitian interface modes with
535 a real spectrum to enable energy localization at user-defined interfaces. This approach maintains efficient energy
536 concentration while significantly expanding the possible locations for harvester installation.

537 In the left and right panels of Fig. 8(c), the localization directions of the two eigenmodes are reversed. By directly
538 connecting these configurations, each consisting of five unit cells, a beam with ten unit cells is formed, creating an
539 interface at the center. As a result, the mode shape becomes a localized mode at the interface, as shown in Fig.
540 12(b). The OBC frequency spectrum remains real and is presented in Fig. 12(a), where all eigenmodes correspond
541 to interface modes localized at the interface. For instance, three eigenmodes corresponding to the starred points
542 in Fig. 12(a) are shown in Fig. 12(b), demonstrating that interface modes span a broad frequency range. This
543 is particularly significant because external energy sources typically operate over a wide range of frequencies. By
544 adjusting the interface position, energy localization can be achieved at user-defined locations. For example, the
545 interface mode is localized at the prescribed interface between the 3rd and 4th unit cells in the left panel of Fig.
546 12(c), between the 5th and 6th unit cells in the middle panel, and between the 7th and 8th unit cells in the right
547 panel. In conclusion, our design potentially enables efficient energy concentration, allows for a user-defined harvester
548 position, and supports energy harvesting over a broad frequency range.

549 6. Conclusion

550 We developed an EMT for nonlocal non-Hermitian Willis metabeams, incorporating sensor-actuator interactions
551 to enable active wave control. Using source-driven homogenization, we derived a dynamic effective medium model
552 that accurately captures high-frequency and short-wavelength wave behavior, overcoming the limitations of classical
553 homogenization approaches. This framework integrates non-Hermitian physics and Willis couplings, allowing precise
554 control over wave amplification, attenuation, and nonreciprocal propagation.

555 Numerical validation through COMSOL simulations confirms the accuracy of our EMT in predicting wave dis-
556 persions and effective material properties. Additionally, we establish a bulk-boundary correspondence for nonlocal
557 non-Hermitian Willis media, linking winding numbers to skin modes and extending topological wave mechanics to
558 elastodynamic systems.

559 Beyond theoretical advancements, we demonstrate applications in nonreciprocal wave control, interface-localized
560 energy harvesting, and low-frequency shear wave manipulation. These findings lay the foundation for active meta-
561 materials with tunable wave properties, opening new possibilities in wave-based computing, vibration control, and
562 energy harvesting.

563 **CRediT authorship contribution statement**

564 Shaoyun Wang: Writing – review & editing, Writing – original draft, Validation, Methodology, Investigation,
 565 Formal analysis, Conceptualization. Guoliang Huang: Writing – review & editing, Validation, Supervision, Funding
 566 acquisition, Formal analysis, Conceptualization, Methodology.

567 **Declaration of Competing Interest**

568 The authors declare no known competing financial interests or personal relationships that could have influenced
 569 the work reported in this paper.

570 **Acknowledgments**

571 The authors thank Dr. Zhanyu Li and Dr. Wen Cheng for their valuable discussions. Guoliang Huang ac-
 572 knowledges support from the Air Force Office of Scientific Research under Grant Nos. AF 9550-18-1-0342 and AF
 573 9550-20-1-0279, with Dr. Byung-Lip (Les) Lee as the Program Manager.

574 **Appendix A. Geometric and material parameters**

575 The geometric parameters of the model in Fig. 2(a) are listed in Table A.1. The background beam is made of
 576 aluminum with a Young's modulus of 70 GPa, a Poisson ratio of 0.33, and a density of 2700 kg/m³. The piezoelectric
 577 patches are composed of PZT-5H, with material properties available in the COMSOL material library. The capacitor
 578 C_0 in Eq. (12) has a value of -0.611 pF.

Table A.1: Geometry parameters of 3D model

Parameter	Value (Unit)	Parameter	Value (Unit)
w	21.9 mm	l	20 mm
w_1	16.1 mm	l_1	12 mm
w_2	8 mm	l_2	4 mm
w_3	3.5 mm	l_3	2.9 mm
h_b	2 mm	h_p	0.5 mm

579 **Appendix B. Green's function**

580 *Appendix B.1. Displacement response in Timoshenko beam*

581 Eliminating M , F , and ψ in the governing equations Eq. (6), we obtain

$$D_0 \frac{\partial^4 w}{\partial x^4} + J_0 \omega^2 \left(1 + \frac{D_0 P_0}{G_0 J_0} \right) \frac{\partial^2 w}{\partial x^2} + \left(\frac{J_0 \rho_0 \omega^4}{G_0} - \rho_0 \omega^2 \right) w = -\frac{\partial q}{\partial x} + \left(1 - \frac{J_0}{G_0} \omega^2 \right) f - \frac{D_0}{G_0} \frac{\partial^2 f}{\partial x^2} + D_0 \frac{\partial^2 p}{\partial x^2} + D_0 \frac{\partial^3 s}{\partial x^3} + J_0 \omega^2 \frac{\partial s}{\partial x} \quad (\text{B.1})$$

582 If only shear force is applied as $f = \delta(x)$, the equations can be reduced as

$$D_0 \frac{\partial^4 w}{\partial x^4} + J_0 \omega^2 \left(1 + \frac{D_0 P_0}{G_0 J_0} \right) \frac{\partial^2 w}{\partial x^2} + \left(\frac{J_0 \rho_0 \omega^4}{G_0} - \rho_0 \omega^2 \right) w = \left(1 - \frac{J_0}{G_0} \omega^2 \right) \delta(x) - \frac{D_0}{G_0} \frac{\partial^2 \delta(x)}{\partial x^2} \quad (\text{B.2})$$

583 The Fourier transform of this equation is

$$w(\omega, k) = \frac{1}{D_0} \frac{1 - \frac{J_0}{G_0} \omega^2 + \frac{D_0}{G_0} k^2}{(k^2 + a^2)(k^2 + b^2)} \quad (\text{B.3})$$

584 Here $a = ik_1$, $b = k_2$, and k_1 (pure real) and k_2 (pure real) satisfy the dispersion relation of Timoshenko beam for a
585 given angular frequency ω

$$\det[\zeta(k, \omega)] = 0. \quad (\text{B.4})$$

586 The inverse Fourier transform using MATLAB symbolic calculation is

$$w(\omega, x) = -\frac{1}{2D_0} \frac{1 - \frac{J_0}{G_0} \omega^2 - \frac{D_0}{G_0} a^2}{(a^2 - b^2)a} e^{-a|x|} + \frac{1}{2D_0} \frac{1 - \frac{J_0}{G_0} \omega^2 - \frac{D_0}{G_0} b^2}{(a^2 - b^2)b} e^{-b|x|} \quad (\text{B.5})$$

587 or equivalently,

$$w(\omega, x) = \frac{1}{2D_0} \frac{1 - \frac{J_0}{G_0} \omega^2 + \frac{D_0}{G_0} k_1^2}{(k_1^2 + k_2^2)ik_1} e^{-ik_1|x|} - \frac{1}{2D_0} \frac{1 - \frac{J_0}{G_0} \omega^2 - \frac{D_0}{G_0} k_2^2}{(k_1^2 + k_2^2)k_2} e^{-k_2|x|} \quad (\text{B.6})$$

588 Smilarily, for delta source q only, the displacement response is

$$w(\omega, x) = \frac{1}{2D_0(k_1^2 + k_2^2)} e^{-ik_1|x|} \text{sgn}(x) - \frac{1}{2D_0(k_1^2 + k_2^2)} e^{-k_2|x|} \text{sgn}(x), \quad (\text{B.7})$$

589 for delta source p only, the displacement response is

$$w(\omega, x) = \frac{ik_1}{2(k_1^2 + k_2^2)} e^{-ik_1|x|} - \frac{k_2}{2(k_1^2 + k_2^2)} e^{-k_2|x|}, \quad (\text{B.8})$$

590 and for delta source s only, the displacement response is

$$w(\omega, x) = -\frac{-D_0 k_1^2 + J_0 \omega^2}{2D_0(k_1^2 + k_2^2)} e^{-ik_1|x|} \text{sgn}(x) + \frac{D_0 k_2^2 + J_0 \omega^2}{2D_0(k_1^2 + k_2^2)} e^{-k_2|x|} \text{sgn}(x) \quad (\text{B.9})$$

591 Appendix B.2. The Green's function

592 Because the system preserves the translational symmetry, applying the linear combination of the four type point
593 load $f_0\delta(x - x')$, $q_0\delta(x - x')$, $p_0\delta(x - x')$, and $s_0\delta(x - x')$ at x' simultaneously, the displacement response function
594 responded at x is

$$\begin{aligned} w(x', x) &= (p_0 A_1 + s_0 \text{sgn}(x - x') A_2 + f_0 A_3 + q_0 \text{sgn}(x - x') A_4) e^{-ik_1|x-x'|} \\ &\quad + (p_0 A_1 a_1 + s_0 \text{sgn}(x - x') A_2 a_2 + f_0 A_3 a_3 + q_0 \text{sgn}(x - x') A_4 a_4) e^{-k_2|x-x'|} \\ &= \mathbf{B}_1(x - x')^T \mathbf{Q}_0 e^{-ik_1|x-x'|} + \mathbf{B}_2(x - x')^T \mathbf{Q}_0 e^{-k_2|x-x'|} \end{aligned} \quad (\text{B.10})$$

595 where

$$\mathbf{B}_1(x) = \begin{bmatrix} A_1 \\ \text{sgn}(x - x') A_2 \\ A_3 \\ \text{sgn}(x - x') A_4 \end{bmatrix}, \quad \mathbf{B}_2(x) = \begin{bmatrix} A_1 a_1 \\ \text{sign}(x - x') A_2 a_2 \\ A_3 a_3 \\ \text{sign}(x) A_4 a_4 \end{bmatrix}, \quad \mathbf{Q}_0 = \begin{bmatrix} p_0 \\ s_0 \\ f_0 \\ q_0 \end{bmatrix}, \quad (\text{B.11})$$

596 and

$$\begin{aligned}
A_1 &= \frac{ik_1}{2(k_1^2 + k_2^2)}, & a_1 &= -\frac{k_2}{ik_1}, \\
A_2 &= \frac{D_0 k_1^2 - J_0 \omega^2}{2D_0(k_1^2 + k_2^2)}, & a_2 &= \frac{D_0 k_2^2 + J_0 \omega^2}{D_0 k_1^2 - J_0 \omega^2}, \\
A_3 &= \frac{1}{2D_0} \frac{1 - \frac{J_0}{G_0} \omega^2 + \frac{D_0}{G_0} k_1^2}{(k_1^2 + k_2^2) ik_1}, & a_3 &= -\frac{ik_1}{k_2} \frac{1 - \frac{J_0}{G_0} \omega^2 - \frac{D_0}{G_0} k_2^2}{1 - \frac{J_0}{G_0} \omega^2 + \frac{D_0}{G_0} k_1^2}, \\
A_4 &= \frac{1}{2D_0(k_1^2 + k_2^2)}, & a_4 &= -1.
\end{aligned} \tag{B.12}$$

597 Meanwhile, the response functions $\psi(x', x)$, $F(x', x)$, and $M(x', x)$ can be assumed as

$$\begin{aligned}
\psi(x', x) &= R_\psi^1(x - x') \mathbf{B}_1(x - x')^T \mathbf{Q}(x') e^{-ik_1|x-x'|} + R_\psi^2(x - x') \mathbf{B}_2(x - x')^T \mathbf{Q}(x') e^{-k_2|x-x'|} \\
F(x', x) &= R_F^1(x - x') \mathbf{B}_1(x - x')^T \mathbf{T} \mathbf{Q}(x') e^{-ik_1|x-x'|} + R_F^2(x - x') \mathbf{B}_2(x - x')^T \mathbf{T} \mathbf{Q}(x') e^{-k_2|x-x'|} \\
M(x', x) &= R_M^1(x - x') \mathbf{B}_1(x - x')^T \mathbf{Q}(x') e^{-ik_1|x-x'|} + R_M^2(x - x') \mathbf{B}_2(x - x')^T \mathbf{Q}(x') e^{-k_2|x-x'|}
\end{aligned} \tag{B.13}$$

598 Inserting them into the first three equations of Eq. (6) with the aid of Eq. (B.10), we obtain the following linear
599 equations

$$\begin{aligned}
-\operatorname{sgn}(x - x') ik_1 R_\psi^1(x - x') + \frac{R_M^1(x - x')}{D_0} &= 0 \\
R_\psi^1(x - x') + \frac{R_F^1(x - x')}{G_0} &= -\operatorname{sgn}(x - x') ik_1 \\
-\operatorname{sgn}(x - x') ik_1 R_F^1(x - x') &= -\rho_0 \omega^2
\end{aligned} \tag{B.14}$$

600 for $R_\psi^1(x - x')$, $R_F^1(x - x')$, $R_M^1(x - x')$, and the linear equations

$$\begin{aligned}
-\operatorname{sgn}(x - x') k_2 R_\psi^2(x - x') + \frac{R_M^2(x - x')}{D_0} &= 0 \\
R_\psi^2(x - x') + \frac{R_F^2(x - x')}{G_0} &= -\operatorname{sgn}(x - x') k_2 \\
-\operatorname{sgn}(x - x') k_2 R_F^2(x - x') &= -\rho_0 \omega^2
\end{aligned} \tag{B.15}$$

601 for $R_\psi^2(x - x')$, $R_F^2(x - x')$, $R_M^2(x - x')$. Solving these equations yields $R_\psi^1(x - x')$, $R_F^1(x - x')$, $R_M^1(x - x')$, as well
602 as $R_\psi^2(x - x')$, $R_F^2(x - x')$, and $R_M^2(x - x')$.

603 Therefore, the Green's function in the frequency domain is

$$\mathbf{G}(\omega, x - x') = \mathbf{R}_1(x - x') \mathbf{B}_1(x - x')^T e^{-ik_1|x-x'|} + \mathbf{R}_2(x - x') \mathbf{B}_2(x - x')^T e^{-k_2|x-x'|} \tag{B.16}$$

604 and

$$\mathbf{R}_1(x) = \begin{bmatrix} R_M^1(x) \\ R_F^1(x) \\ 1 \\ R_\psi^1(x) \end{bmatrix}, \quad \mathbf{R}_2(x) = \begin{bmatrix} R_M^2(x) \\ R_F^2(x) \\ 1 \\ R_\psi^2(x) \end{bmatrix}. \tag{B.17}$$

605 And the state vector response $\mathbf{u}(x)$ at x , excited by a source vector $\mathbf{Q}(x')$ at x' , is given by

$$\mathbf{u}(x) = \int \mathbf{G}(\omega, x - x') \mathbf{Q}(x') dx'. \quad (\text{B.18})$$

606 Appendix C. Symmetry conditions of Green's function

607 As shown in the middle panel of Fig. 2(b), the periodic actuators can be regarded as periodic scatterers, inducing
 608 multiple scattering effects. To account for these effects, we construct the Green's function of the background beam
 609 and analyze its symmetry. The Green's function for Eq. (6) satisfies

$$\zeta_1 \mathbf{G}(x - x') = \delta(x - x') \mathbf{I} \quad (\text{C.1})$$

610 where the analytical expression of Green's function is presented in [Appendix B](#). Using the Fourier transform

$$G_{ij}(\omega, k) = \frac{1}{\sqrt{2\pi}} \int_{-\infty}^{\infty} G_{ij}(\omega, x - x') e^{ik(x-x')} d(x - x'), \quad i, j = 1, 2, 3, 4. \quad (\text{C.2})$$

611 We find the corresponding Green's function $\mathbf{G}(\omega, k)$ in the frequency-wavenumber domain satisfies

$$\zeta(\omega, k) \mathbf{G}(\omega, k) = \mathbf{I}. \quad (\text{C.3})$$

612 It is evident that $\zeta(\omega, k)$ satisfies $\zeta(\omega, k) = \zeta^\dagger(\omega, k)$, $\zeta(\omega, k) = \zeta^T(\omega, -k)$, and $\zeta(\omega, k) = \zeta^*(-\omega, -k)$. Consequently,
 613 the Green's function $\mathbf{G}(\omega, k)$ also satisfies the Hermitian condition for given ω and k

$$\mathbf{G}(\omega, k) = \mathbf{G}^\dagger(\omega, k), \quad \mathbf{G}(\omega, k) = \mathbf{G}^T(\omega, -k), \quad \mathbf{G}(\omega, k) = \mathbf{G}^*(-\omega, -k) \quad (\text{C.4})$$

614 Using the inverse Fourier transform

$$G_{ij}(\omega, x - x') = \frac{1}{\sqrt{2\pi}} \int_{-\infty}^{\infty} G_{ij}(\omega, k) e^{ik(x-x')} dk, \quad i, j = 1, 2, 3, 4, \quad (\text{C.5})$$

615 the Green's function $\mathbf{G}(\omega, x - x')$ satisfies the following symmetry

$$\mathbf{G}(\omega, x - x') = \mathbf{G}^\dagger(\omega, x - x'), \quad \mathbf{G}(\omega, x - x') = \mathbf{G}^T(\omega, x' - x), \quad \mathbf{G}(\omega, x - x') = \mathbf{G}^*(-\omega, x' - x) \quad (\text{C.6})$$

616 Appendix D. Derivation of effective constitutive relations

617 The ζ is not a singular matrix in general, so Eq. (22) can be rewritten as

$$\mathbf{u}_{\text{ext}} = \mathbf{u}_{\text{eff}} + \zeta^{-1} \mathbf{Q}_{\text{eff}}. \quad (\text{D.1})$$

618 In addition, through the elimination of the local source vector \mathbf{Q}_0 in Eq. (23) and Eq. (24), we find

$$\beta \mathbf{u}_{\text{ext}} = (\mathbf{I} - \beta \mathbf{S}) \mathbf{Q}_{\text{eff}} l. \quad (\text{D.2})$$

⁶¹⁹ Subtracting Eq. (D.2) by the product of β to Eq. (D.1) gives

$$\beta (\mathbf{u}_{\text{eff}} + \zeta^{-1} \mathbf{Q}_{\text{eff}}) = (\mathbf{I} - \beta \mathbf{S}) \mathbf{Q}_{\text{eff}} l \quad (\text{D.3})$$

⁶²⁰ Reorganizing yields the effective constitutive relations in Eq. (25)

$$\mathbf{Q}_{\text{eff}} = [(\mathbf{I} - \beta \mathbf{S}) l - \beta \zeta^{-1}]^{-1} \beta \mathbf{u}_{\text{eff}} \quad (\text{D.4})$$

⁶²¹ Appendix E. Retrieval of local polarizability tensor

⁶²² Due to the complexity of the unit cell geometry, accurately relating the local polarizability tensor β to the transfer
⁶²³ functions $H_1(\omega)$ and $H_2(\omega)$ analytically is challenging. In this section, we employ a retrieval method to numerically
⁶²⁴ extract the local polarizability tensor, as illustrated in Fig. 3(a). The local state vector \mathbf{u}_{loc} is directly obtained from
⁶²⁵ COMSOL, while the local source vector \mathbf{Q} is extracted using the scattering method. For each test, given the known
⁶²⁶ \mathbf{u}_{loc} and \mathbf{Q} , we obtain four equations from Eq. (11) with β as the unknown. Since the polarizability tensor contains
⁶²⁷ 16 unknowns, four independent scattering tests are conducted to construct a system of 16 equations, enabling the
⁶²⁸ unique determination of these unknowns.

⁶²⁹ Appendix E.1. Numerical extraction of the local source vector

⁶³⁰ Here, we utilize the extracted displacement field in the frequency domain to inversely determine the local source
⁶³¹ vector \mathbf{Q} . A unit cell is embedded in the middle of the background beam, with perfect matching layers on both
⁶³² sides (not shown). A unit transverse force is applied at a specified position in the background beam, as illustrated
⁶³³ in Fig. 3(a). In this section, we use asymmetric constant transfer function with $H_1(\omega) = 0.35$ and $H_2(\omega) = -0.25$.
⁶³⁴ According to Eq. (B.10), the analytical displacement response function at position x for an excitation applied at the
⁶³⁵ origin is given by

$$w(0, x) = \mathbf{B}_1(x)^T \mathbf{Q}_0 e^{-ik_1|x|} + \mathbf{B}_2(x)^T \mathbf{Q}_0 e^{-k_2|x|}. \quad (\text{E.1})$$

⁶³⁶ Meanwhile, the scattered displacement field is extracted from COMSOL. For each test, we perform two simulations:
⁶³⁷ one with the transfer function set to zero and another with a nonzero transfer function. The scattered displacement
⁶³⁸ field is then obtained by subtracting the displacement field of the zero-transfer-function case from that of the nonzero-
⁶³⁹ transfer-function case. For the i th test, we acquire the scattered displacement vector $\mathbf{w}^i = [w^i(0, x_1), \dots, w^i(0, x_N)]^T$
⁶⁴⁰ at positions $\mathbf{x} = [x_1, x_2, \dots, x_N]^T$. At each position, Eq. (E.1) must be satisfied, leading to

$$\begin{aligned} & \left[\mathbf{B}_1(x_1)^T e^{-ik_1|x_1|} + \mathbf{B}_2(x_1)^T e^{-k_2|x_1|} \right] \mathbf{Q}^i = w^i(0, x_1) \\ & \left[\mathbf{B}_1(x_2)^T e^{-ik_1|x_2|} + \mathbf{B}_2(x_2)^T e^{-k_2|x_2|} \right] \mathbf{Q}^i = w^i(0, x_2) \\ & \quad \dots \\ & \left[\mathbf{B}_1(x_N)^T e^{-ik_1|x_N|} + \mathbf{B}_2(x_N)^T e^{-k_2|x_N|} \right] \mathbf{Q}^i = w^i(0, x_N). \end{aligned} \quad (\text{E.2})$$

⁶⁴¹ Here, N is chosen to be greater than 4, and \mathbf{Q}^i is determined using the least squares method. To achieve the desired
⁶⁴² precision, a large integer N (2000 in this study) is selected. By solving the overdetermined system using the least

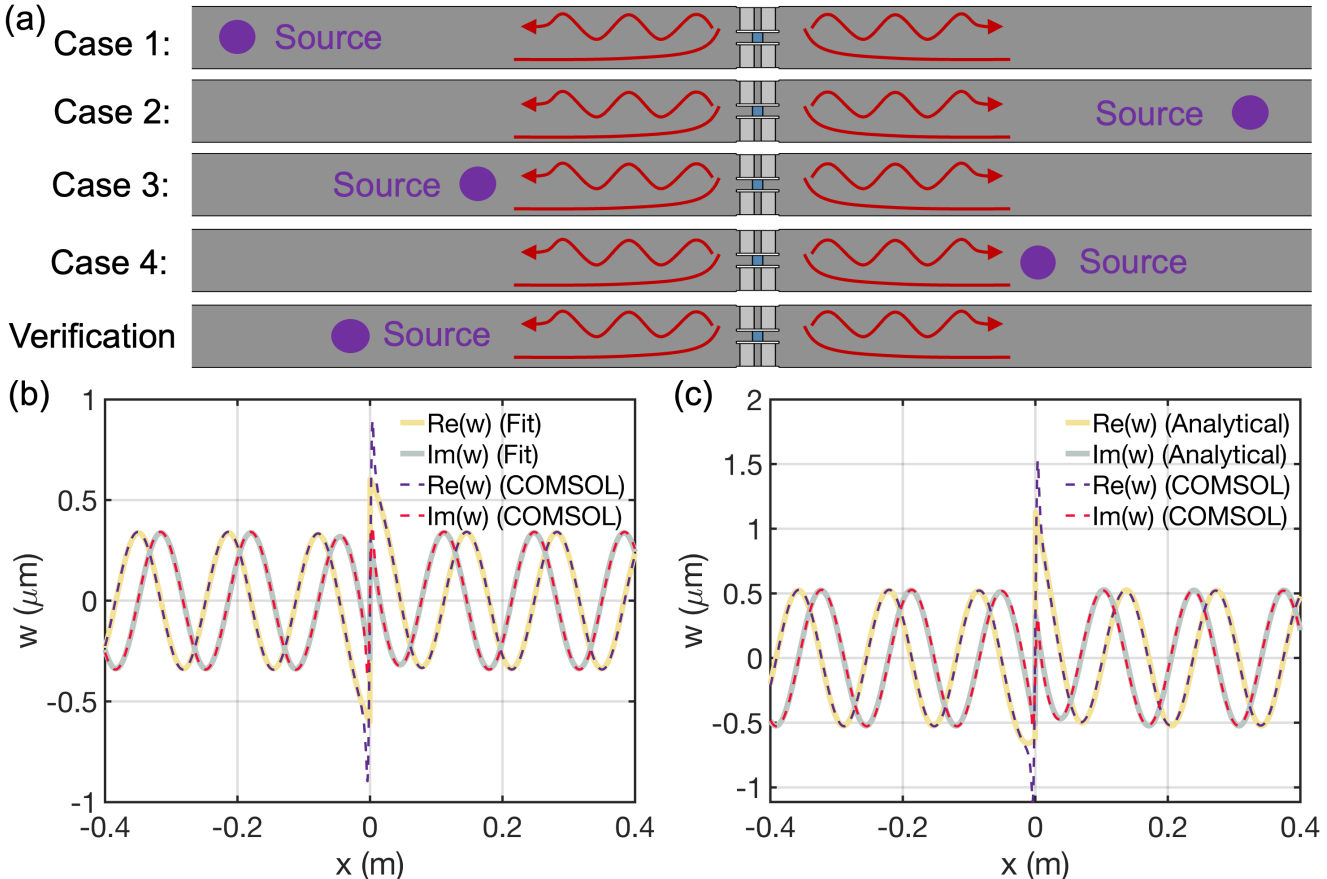


Figure E.13: Numerical extraction of the polarizability tensor. (a) Four numerical tests for extracting the polarizability tensor, along with an additional case for verification. (b) Real part (purple dashed line) and imaginary part (red dashed line) of the scattered displacement field from COMSOL simulations for the first case in (a), compared with the fitted response of a point source (yellow solid line for the real part and gray solid line for the imaginary part). (c) Real part (purple dashed line) and imaginary part (red dashed line) of the scattered displacement field from COMSOL simulations for the verification case in (a), compared with the analytical response of a point source derived from the four tests in (a) (yellow solid line for the real part and gray solid line for the imaginary part).

squares method, we obtain

$$\mathbf{Q}^i = \mathcal{G}^{-1} \mathbf{w}^i \quad (\text{E.3})$$

where $(\cdot)^{-1}$ denotes the Moore–Penrose pseudoinverse, and the rectangular matrix \mathcal{G} is defined as

$$\mathcal{G} = \begin{bmatrix} \mathbf{B}_1(x_1)^T e^{-ik_1|x_1|} + \mathbf{B}_2(x_1)^T e^{-ik_2|x_1|} \\ \mathbf{B}_1(x_2)^T e^{-ik_1|x_2|} + \mathbf{B}_2(x_2)^T e^{-ik_2|x_2|} \\ \vdots \\ \mathbf{B}_1(x_N)^T e^{-ik_1|x_N|} + \mathbf{B}_2(x_N)^T e^{-ik_2|x_N|} \end{bmatrix} \quad (\text{E.4})$$

To assess the accuracy of the inverse extraction, we compare the analytical scattered displacement field, computed using Eq. (E.1) with the inversely obtained \mathbf{Q}^i , against the scattered displacement field extracted from the COMSOL simulation for the first case, as shown in Fig. 3(b). The real and imaginary parts of both results closely match, except in the region very close to the unit cell, where microstructural effects become significant. This confirms that the point source assumption is valid for our study and that the inverse extraction method is reliable.

650 Appendix E.2. Numerical extraction of the polarizability tensor

651 Now we have four local source vectors for four tests. The four local state vectors can be extracted in COMOSL
652 directly. Therefore, for these four tests, the following condition is satisfied according to Eq. (11)

$$\mathbf{Q}^i = \boldsymbol{\beta} \mathbf{u}_{\text{loc}}^i, \quad i = 1, 2, 3, 4, \quad (\text{E.5})$$

653 These linear equations can also be expressed as:

$$\mathbf{Q}^i = u_{\text{loc}}^i(1)\boldsymbol{\beta}_1 + u_{\text{loc}}^i(2)\boldsymbol{\beta}_2 + u_{\text{loc}}^i(3)\boldsymbol{\beta}_3 + u_{\text{loc}}^i(4)\boldsymbol{\beta}_4, \quad i = 1, 2, 3, 4, \quad (\text{E.6})$$

654 where $\boldsymbol{\beta}_j$ ($j = 1, 2, 3, 4$) is the j th column vector of the matrix $\boldsymbol{\beta}$, and $u_{\text{loc}}^i(j)$ ($j = 1, 2, 3, 4$) is the j th element of the
655 vector $\mathbf{u}_{\text{loc}}^i$. Eq. (E.6) can be reformulated as:

$$\begin{bmatrix} \mathbf{Q}^1 \\ \mathbf{Q}^2 \\ \mathbf{Q}^3 \\ \mathbf{Q}^4 \end{bmatrix} = \begin{bmatrix} u_{\text{loc}}^1(1)\mathbf{I} & u_{\text{loc}}^1(2)\mathbf{I} & u_{\text{loc}}^1(3)\mathbf{I} & u_{\text{loc}}^1(4)\mathbf{I} \\ u_{\text{loc}}^2(1)\mathbf{I} & u_{\text{loc}}^2(2)\mathbf{I} & u_{\text{loc}}^2(3)\mathbf{I} & u_{\text{loc}}^2(4)\mathbf{I} \\ u_{\text{loc}}^3(1)\mathbf{I} & u_{\text{loc}}^3(2)\mathbf{I} & u_{\text{loc}}^3(3)\mathbf{I} & u_{\text{loc}}^3(4)\mathbf{I} \\ u_{\text{loc}}^4(1)\mathbf{I} & u_{\text{loc}}^4(2)\mathbf{I} & u_{\text{loc}}^4(3)\mathbf{I} & u_{\text{loc}}^4(4)\mathbf{I} \end{bmatrix} \begin{bmatrix} \boldsymbol{\beta}_1 \\ \boldsymbol{\beta}_2 \\ \boldsymbol{\beta}_3 \\ \boldsymbol{\beta}_4 \end{bmatrix}, \quad (\text{E.7})$$

656 where \mathbf{I} is the 4×4 identity matrix. We concatenate \mathbf{Q}^i and $\boldsymbol{\beta}_i$ ($i = 1, 2, 3, 4$) to form larger vectors and assemble
657 $\mathbf{u}_{\text{loc}}^i$ ($i = 1, 2, 3, 4$) into a matrix

$$\mathbf{Q} = \begin{bmatrix} \mathbf{Q}^1 \\ \mathbf{Q}^2 \\ \mathbf{Q}^3 \\ \mathbf{Q}^4 \end{bmatrix}, \quad \mathbf{u}_{\text{loc}} = \begin{bmatrix} (\mathbf{u}_{\text{loc}}^1)^T \\ (\mathbf{u}_{\text{loc}}^2)^T \\ (\mathbf{u}_{\text{loc}}^3)^T \\ (\mathbf{u}_{\text{loc}}^4)^T \end{bmatrix}, \quad \mathcal{B} = \begin{bmatrix} \boldsymbol{\beta}_1 \\ \boldsymbol{\beta}_2 \\ \boldsymbol{\beta}_3 \\ \boldsymbol{\beta}_4 \end{bmatrix}. \quad (\text{E.8})$$

658 Then Eq. (E.7) can be expressed as

$$\mathbf{Q} = \mathbf{u}_{\text{loc}} \otimes \mathbf{I} \mathcal{B}, \quad (\text{E.9})$$

659 where \otimes is the Kronecker product. Solving for \mathcal{B} , we obtain

$$\mathcal{B} = (\mathbf{u}_{\text{loc}} \otimes \mathbf{I})^{-1} \mathbf{Q} \quad (\text{E.10})$$

660 Finally, the local polarizability matrix $\boldsymbol{\beta}$ is obtained by rearranging the elements of the vector \mathcal{B} . Since the polar-
661 izability matrix is generally frequency-dependent, we conduct these four tests at different frequencies and derive the
662 frequency-dependent polarizability matrix function through curve fitting.

663 Finally, we verify the local polarizability matrix $\boldsymbol{\beta}$ through a validation test, as shown in the bottom panel of
664 Fig. 3(a). In this case, the source position differs from those in the four previous cases. First, the local state
665 vector is extracted, and then the local source vector is determined by multiplying the local state vector by the local
666 polarizability matrix. Using Eq. (E.1), the analytical scattered displacement field is then computed for the obtained
667 local source vector. This analytical result is compared with the scattered displacement field extracted from the

668 COMSOL simulation in Fig. 3(c). The consistency between the two results confirms the validity of the point source
 669 assumption and the reliability of the retrieval method for determining the polarizability matrix.

670 Appendix F. Interpretation of nonlocal effective parameters

671 According to our effective medium theory, the effective parameters in Eq. (25) depend on both frequency and
 672 wavenumber. However, for freely propagating waves, frequency and wavenumber are not independent but must satisfy
 673 the dispersion relation given in Eq. (47). This implies that the effective parameters are physically meaningful only
 674 at frequencies and wavenumbers that lie on the dispersion curves corresponding to freely traveling waves. This raises
 675 an apparent paradox: whether the effective parameters remain meaningful for arbitrary frequency and wavenumber,
 676 or whether the assumption of independent frequency and wavenumber in the effective parameters requires further
 677 justification.

678 To treat frequency and wavenumber as independent variables, we must consider waves under external excitation.
 679 We begin by introducing a traveling wave excitation of the form

$$\mathbf{Q}_{\text{ext}}(x, t) = \mathbf{Q}_{\text{ext}}(\omega, k)e^{i(kx - \omega t)} \quad (\text{F.1})$$

680 where $\mathbf{Q}_{\text{ext}}(\omega, k)$ represents the amplitude, which depends on both frequency and wavenumber. The solution to Eq.
 681 (43) can then be expressed as

$$\mathbf{u}_{\text{eff}}(x, t) = \mathbf{u}_{\text{eff}}(\omega, k)e^{i(kx - \omega t)} \quad (\text{F.2})$$

682 where the amplitude vector satisfies

$$\mathbf{u}_{\text{eff}}(\omega, k) = \mathbf{H}(\omega, k)^{-1}\mathbf{Q}_{\text{ext}}(\omega, k). \quad (\text{F.3})$$

683 If the frequency and wavenumber satisfy the dispersion relation, $\mathbf{H}(\omega, k)$ becomes singular, causing the amplitude vec-
 684 tor to diverge, similar to resonance in vibrational systems. To eliminate this singularity, damping can be introduced
 685 into the system, ensuring that the amplitude vector remains finite. Conversely, if the frequency and wavenumber do
 686 not satisfy the dispersion relation, $\mathbf{H}(\omega, k)$ remains nonsingular, and the amplitude vector is naturally finite. In this
 687 case, the amplitude vector depends on $\mathbf{H}(\omega, k)$, which in turn is determined by the effective parameters, allowing
 688 frequency and wavenumber to be treated as independent variables.

689 Next, we consider a more realistic harmonic excitation of the form

$$\mathbf{Q}_{\text{ext}}(x, t) = \mathbf{Q}_{\text{ext}}(\omega, x)e^{-i\omega t}, \quad (\text{F.4})$$

690 which can be expanded as

$$\mathbf{Q}_{\text{ext}}(x, t) = \frac{e^{-i\omega t}}{\sqrt{2\pi}} \int_{-\infty}^{\infty} \mathbf{Q}_{\text{ext}}(\omega, k)e^{ikx} dk. \quad (\text{F.5})$$

691 For each Fourier component $\mathbf{Q}_{\text{ext}}(\omega, k)$, the corresponding response is given by $\mathbf{u}_{\text{eff}}(\omega, k)$. Using the principle of
 692 superposition, the total response can be written as

$$\mathbf{u}_{\text{eff}}(x, t) = \frac{e^{-i\omega t}}{\sqrt{2\pi}} \int_{-\infty}^{\infty} \mathbf{H}(\omega, k)^{-1}\mathbf{Q}_{\text{ext}}(\omega, k)e^{ikx} dk. \quad (\text{F.6})$$

693 This result shows that the state vector response depends on the effective parameters for arbitrary frequency and
694 wavenumber. Therefore, in the context of excitation problems, frequency and wavenumber can be treated as inde-
695 pendent variables. Furthermore, this approach offers greater flexibility in modulating the effective parameters, as
696 both frequency and wavenumber can be controlled. For example, a gradient medium with slowly varying properties
697 can be designed using the WKB approximation to develop an elastic ray theory, enabling novel wave propagation
698 phenomena ([Wang et al., 2023](#)).

699 **References**

- 700 Agranovich, V. M. and Ginzburg, V. (2013). *Crystal optics with spatial dispersion, and excitons*, volume 42. Springer
701 Science & Business Media.
- 702 Altman, C. and Suchy, K. (2011). *Reciprocity, spatial mapping and time reversal in electromagnetics*. Springer
703 Science & Business Media.
- 704 Alù, A. (2011). First-principles homogenization theory for periodic metamaterials. *Physical Review B—Condensed
705 Matter and Materials Physics*, 84(7):075153.
- 706 Ashida, Y., Gong, Z., and Ueda, M. (2020). Non-hermitian physics. *Advances in Physics*, 69(3):249–435.
- 707 Baz, A. (2024). Why active willis metamaterials? a controllability and observability perspective. *The Journal of the
708 Acoustical Society of America*, 156(5):3338–3352.
- 709 Bender, C. M. and Boettcher, S. (1998). Real spectra in non-hermitian hamiltonians having p t symmetry. *Physical
710 review letters*, 80(24):5243.
- 711 Bender, C. M. and Hook, D. W. (2024). Pt-symmetric quantum mechanics. *Reviews of Modern Physics*, 96(4):045002.
- 712 Chen, Y. and Haberman, M. R. (2023). Controlling displacement fields in polar willis solids via gauge transformations.
713 *Physical Review Letters*, 130(14):147201.
- 714 Chen, Y., Li, X., Hu, G., Haberman, M. R., and Huang, G. (2020). An active mechanical willis meta-layer with
715 asymmetric polarizabilities. *Nature communications*, 11(1):3681.
- 716 Chen, Y., Li, X., Scheibner, C., Vitelli, V., and Huang, G. (2021). Realization of active metamaterials with odd
717 micropolar elasticity. *Nature communications*, 12(1):5935.
- 718 Cheng, W. and Hu, G. (2022). Acoustic skin effect with non-reciprocal willis materials. *Applied Physics Letters*,
719 121(4).
- 720 Christensen, J., Haberman, M. R., Srivastava, A., Huang, G., and Shmuel, G. (2024). Perspective on non-hermitian
721 elastodynamics. *Applied Physics Letters*, 125(23).
- 722 Galiffi, E., Tirole, R., Yin, S., Li, H., Vezzoli, S., Huidobro, P. A., Silveirinha, M. G., Sapienza, R., Alù, A., and
723 Pendry, J. B. (2022). Photonics of time-varying media. *Advanced Photonics*, 4(1):014002–014002.

- 724 Goldstein, H., Poole, C., and Safko, J. (2002). *Classical Mechanics*. Addison Wesley.
- 725 Huang, H., Sun, C., and Huang, G. (2009). On the negative effective mass density in acoustic metamaterials.
- 726 *International Journal of Engineering Science*, 47(4):610–617.
- 727 Jackson, J. (2012). *Classical Electrodynamics*. Wiley.
- 728 Landau, L., Landau, L., Lifshits, E., Kosevich, A., Lifshitz, E., and Pitaevskii, L. (1986). *Theory of Elasticity: Volume 7*. Course of theoretical physics. Butterworth-Heinemann.
- 730 Landau, L., Lifshitz, E., and Sykes, J. (1976). *Mechanics: Volume 1*. Course of theoretical physics. Butterworth-Heinemann.
- 732 Lee, J.-H., Zhang, Z., and Gu, G. X. (2023). Dynamic homogenization of heterogeneous piezoelectric media: a polarization approach using infinite-body green's function. *Journal of the Mechanics and Physics of Solids*, 181:105442.
- 734 Li, J., Shen, C., Díaz-Rubio, A., Tretyakov, S. A., and Cummer, S. A. (2018). Systematic design and experimental demonstration of bianisotropic metasurfaces for scattering-free manipulation of acoustic wavefronts. *Nature communications*, 9(1):1342.
- 737 Li, Z., Han, P., and Hu, G. (2024). Willis dynamic homogenization method for acoustic metamaterials based on multiple scattering theory. *Journal of the Mechanics and Physics of Solids*, 189:105692.
- 739 Li, Z., Qu, H., Zhang, H., Liu, X., and Hu, G. (2022). Interfacial wave between acoustic media with willis coupling.
- 740 *Wave Motion*, 112:102922.
- 741 Liu, Y., Liang, Z., Zhu, J., Xia, L., Mondain-Monval, O., Brunet, T., Alù, A., and Li, J. (2019). Willis metamaterial on a structured beam. *Physical Review X*, 9(1):011040.
- 743 Milton, G. W. (2007). New metamaterials with macroscopic behavior outside that of continuum elastodynamics.
- 744 *New Journal of Physics*, 9(10):359.
- 745 Milton, G. W., Briane, M., and Willis, J. R. (2006). On cloaking for elasticity and physical equations with a transformation invariant form. *New journal of physics*, 8(10):248.
- 747 Milton, G. W. and Willis, J. R. (2010). Minimum variational principles for time-harmonic waves in a dissipative medium and associated variational principles of hashin–shtrikman type. *Proceedings of the Royal Society A: Mathematical, Physical and Engineering Sciences*, 466(2122):3013–3032.
- 750 Miri, M.-A. and Alu, A. (2019). Exceptional points in optics and photonics. *Science*, 363(6422):eaar7709.
- 751 Muhafra, K., Haberman, M. R., and Shmuel, G. (2023). Discrete one-dimensional models for the electromomentum coupling. *Physical Review Applied*, 20(1):014042.
- 753 Muhlestein, M. B., Sieck, C. F., Wilson, P. S., and Haberman, M. R. (2017). Experimental evidence of willis coupling in a one-dimensional effective material element. *Nature communications*, 8(1):15625.

- 755 Nassar, H., He, Q.-C., and Auffray, N. (2015). Willis elastodynamic homogenization theory revisited for periodic
756 media. *Journal of the Mechanics and Physics of Solids*, 77:158–178.
- 757 Nassar, H., He, Q.-C., and Auffray, N. (2016). On asymptotic elastodynamic homogenization approaches for periodic
758 media. *Journal of the Mechanics and Physics of Solids*, 88:274–290.
- 759 Nassar, H., Yousefzadeh, B., Fleury, R., Ruzzene, M., Alù, A., Daraio, C., Norris, A. N., Huang, G., and Haberman,
760 M. R. (2020). Nonreciprocity in acoustic and elastic materials. *Nature Reviews Materials*, 5(9):667–685.
- 761 Nemat-Nasser, S. and Srivastava, A. (2011). Overall dynamic constitutive relations of layered elastic composites.
762 *Journal of the Mechanics and Physics of Solids*, 59(10):1953–1965.
- 763 Norris, A. N., Shuvalov, A., and Kutsenko, A. (2012). Analytical formulation of three-dimensional dynamic homoge-
764 nization for periodic elastic systems. *Proceedings of the Royal Society A: Mathematical, Physical and Engineering
765 Sciences*, 468(2142):1629–1651.
- 766 Okuma, N., Kawabata, K., Shiozaki, K., and Sato, M. (2020). Topological origin of non-hermitian skin effects.
767 *Physical review letters*, 124(8):086801.
- 768 Pernas-Salomón, R., Haberman, M. R., Norris, A. N., and Shmuel, G. (2021). The electromomentum effect in
769 piezoelectric willis scatterers. *Wave Motion*, 106:102797.
- 770 Pernas-Salomón, R. and Shmuel, G. (2018). Dynamic homogenization of composite and locally resonant flexural
771 systems. *Journal of the Mechanics and Physics of Solids*, 119:43–59.
- 772 Pernas-Salomón, R. and Shmuel, G. (2020a). Fundamental principles for generalized willis metamaterials. *Physical
773 Review Applied*, 14(6):064005.
- 774 Pernas-Salomón, R. and Shmuel, G. (2020b). Symmetry breaking creates electro-momentum coupling in piezoelectric
775 metamaterials. *Journal of the Mechanics and Physics of Solids*, 134:103770.
- 776 Ponge, M.-F., Poncelet, O., and Torrent, D. (2017). Dynamic homogenization theory for nonlocal acoustic metama-
777 terials. *Extreme Mechanics Letters*, 12:71–76.
- 778 Qu, H., Liu, X., and Hu, G. (2022). Mass-spring model of elastic media with customizable willis coupling. *Internation-
779 al Journal of Mechanical Sciences*, 224:107325.
- 780 Rabczuk, T., Ren, H., and Zhuang, X. (2023). Computational methods based on peridynamics and nonlocal operators.
781 In *Computational Methods in Engineering & the Sciences*. Springer.
- 782 Sakurai, J. and Napolitano, J. (2017). *Modern Quantum Mechanics*. Cambridge University Press.
- 783 Shokri, B. and Rukhadze, A. A. (2019). *Electrodynamics of Conducting Dispersive Media*. Springer.
- 784 Shore, R. A. and Yaghjian, A. D. (2007). Traveling waves on two-and three-dimensional periodic arrays of lossless
785 scatterers. *Radio Science*, 42(06):1–40.

- 786 Shuvalov, A., Kutsenko, A., Norris, A., and Poncelet, O. (2011). Effective willis constitutive equations for periodically
787 stratified anisotropic elastic media. *Proceedings of the Royal Society A: Mathematical, Physical and Engineering*
788 *Sciences*, 467(2130):1749–1769.
- 789 Sieck, C. F., Alù, A., and Haberman, M. R. (2017). Origins of willis coupling and acoustic bianisotropy in acoustic
790 metamaterials through source-driven homogenization. *Physical Review B*, 96(10):104303.
- 791 Srivastava, A. (2015). Elastic metamaterials and dynamic homogenization: a review. *International Journal of Smart*
792 *and Nano Materials*, 6(1):41–60.
- 793 Wang, S., Hu, Z., Wu, Q., Chen, H., Prodan, E., Zhu, R., and Huang, G. (2023). Smart patterning for topological
794 pumping of elastic surface waves. *Science Advances*, 9(30):eadh4310.
- 795 Wang, S., Shao, N., Chen, H., Chen, J., Qian, H., Wu, Q., Duan, H., Alu, A., and Huang, G. (2025). Temporal
796 refraction and reflection in modulated mechanical metabeams: theory and physical observation. *arXiv preprint*
797 *arXiv:2501.09989*.
- 798 Wang, Y., Wu, Q., Tian, Y., and Huang, G. (2024). Non-hermitian wave dynamics of odd plates: Microstructure
799 design and theoretical modelling. *Journal of the Mechanics and Physics of Solids*, 182:105462.
- 800 Willis, J. R. (1981). Variational principles for dynamic problems for inhomogeneous elastic media. *Wave Motion*,
801 3(1):1–11.
- 802 Willis, J. R. (1997). Dynamics of composites. In *Continuum micromechanics*, pages 265–290. Springer.
- 803 Willis, J. R. (2009). Exact effective relations for dynamics of a laminated body. *Mechanics of Materials*, 41(4):385–
804 393.
- 805 Willis, J. R. (2011). Effective constitutive relations for waves in composites and metamaterials. *Proceedings of the*
806 *Royal Society A: Mathematical, Physical and Engineering Sciences*, 467(2131):1865–1879.
- 807 Willis, J. R. (2012). The construction of effective relations for waves in a composite. *Comptes rendus. Mécanique*,
808 340(4-5):181–192.
- 809 Wu, Q., Wang, S., Qian, H., Wang, Y., and Huang, G. (2024). Understanding of topological mode and skin mode
810 morphing in 1d and 2d non-hermitian resonance-based meta-lattices. *Journal of the Mechanics and Physics of*
811 *Solids*, 193:105907.
- 812 Wu, Q., Xu, X., Qian, H., Wang, S., Zhu, R., Yan, Z., Ma, H., Chen, Y., and Huang, G. (2023). Active metamaterials
813 for realizing odd mass density. *Proceedings of the National Academy of Sciences*, 120(21):e2209829120.
- 814 Wu, Q., Zhang, X., Shivashankar, P., Chen, Y., and Huang, G. (2022). Independent flexural wave frequency
815 conversion by a linear active metalayer. *Physical Review Letters*, 128(24):244301.
- 816 Xia, Y., Riva, E., Rosa, M. I., Cazzulani, G., Erturk, A., Braghin, F., and Ruzzene, M. (2021). Experimental
817 observation of temporal pumping in electromechanical waveguides. *Physical Review Letters*, 126(9):095501.

- 818 Yang, Z., Zhang, K., Fang, C., and Hu, J. (2020). Non-hermitian bulk-boundary correspondence and auxiliary
819 generalized brillouin zone theory. *Physical Review Letters*, 125(22):226402.
- 820 Yao, S. and Wang, Z. (2018). Edge states and topological invariants of non-hermitian systems. *Physical review
821 letters*, 121(8):086803.
- 822 Yao, W., Zhong, W., and Lim, C. W. (2009). *Symplectic elasticity*. World Scientific.
- 823 Yokomizo, K. and Murakami, S. (2019). Non-bloch band theory of non-hermitian systems. *Physical review letters*,
824 123(6):066404.
- 825 Yves, S., Fleury, R., Shmuel, G., Fruchart, M., Vitelli, V., Haberman, M. R., and Alù, A. (2024). Symmetry-driven
826 phononic metamaterials. *arXiv preprint arXiv:2411.18556*.
- 827 Zhai, Y., Kwon, H.-S., and Popa, B.-I. (2019). Active willis metamaterials for ultracompact nonreciprocal linear
828 acoustic devices. *Physical Review B*, 99(22):220301.
- 829 Zhang, K., Yang, Z., and Fang, C. (2020). Correspondence between winding numbers and skin modes in non-hermitian
830 systems. *Physical Review Letters*, 125(12):126402.
- 831 Zhu, R., Liu, X., Hu, G., Sun, C., and Huang, G. (2014). Negative refraction of elastic waves at the deep-
832 subwavelength scale in a single-phase metamaterial. *Nature communications*, 5(1):5510.